

Friedrich Schiller Universität Jena  
PAF

Dissertation

**High-Fluence Ion Beam  
Irradiation of Semiconductor  
Nanowires**

Andreas Johannes

July 2015

# Theses of the Dissertation

1. Semiconductor nanowires are a suitable model system to investigate the interaction between energetic ions and nanostructures.
2. The Sigmund sputtering model is a good approximation for the sputtering in nanostructures. It explains the qualitative structure-size dependence of the sputter yield.
3. Sputtering from nanostructures is comparable in experiments and simulations with the program *iradina*, a Monte-Carlo simulation tool based on the binary collision approximation.
4. The nanowire diameter and/or ion energy dependent sputter yield from nanowires is maximum where the nanowire diameter is equal to the projected range of the ion in the nanowire material.
5. The redeposition from the substrate onto upstanding nanowires is negligible compared to the sputtering from the nanowires. The fluence of atoms redeposited from the substrate onto the nanowire can be estimated to be around  $0.1 \cdot SY \cdot \Phi$ , with  $SY$  the sputter yield from the substrate surface.
6. Sputtering in nanostructures leads to a non-linear increase in the doping concentration with high irradiated ion fluences. This can be quantified by nano-XRF.
7. Static simulations are useful to predict doping concentrations up to an ion fluence where 20% of the total volume effected by the ion beam is sputtered. This fluence may be significantly lower in nanostructures than in bulk, because of the enhanced sputtering in nanostructures.
8. *Si* nanowires show plastic deformation when irradiated with 100 and 300 keV  $Ar^+$  ions at room-temperature.
9. The deformation of *Si* nanowires by room temperature ion irradiation is not caused by point defects and is not oriented along the ion beam direction, the nanowires always become shorter.
10. A FIB system equipped with a micro-manipulator is a fun tool to manipulate and manufacture useful nanowire samples.

# Contents

<b>1</b>	<b>Introduction</b>	<b>1</b>
<b>2</b>	<b>Background</b>	<b>2</b>
2.1	Ion-solid interactions . . . . .	2
2.2	Simulation of ion-solid interaction . . . . .	9
<b>3</b>	<b>Experimental Methods</b>	<b>16</b>
3.1	Nanowire synthesis . . . . .	16
3.2	Modification . . . . .	18
3.3	Characterization . . . . .	20
<b>4</b>	<b>High Doping Concentrations in Nanowires</b>	<b>25</b>
4.1	Doping and Sputtering . . . . .	25
4.2	nano-XRF on single nanowires . . . . .	26
4.3	Pseudo-dynamic simulation . . . . .	31
4.4	Summarizing Discussion . . . . .	34
<b>5</b>	<b>Conclusions and Outlook</b>	<b>37</b>

# **1 Introduction**

# 2 Background

This chapter will provide a general scientific context for this dissertation. First, a general outline of energetic ion-solid interaction is given. Next, the effects of the interaction between the ion and the electrons in the solid are discussed separately from the collisions of the ion with nuclei in the solid. With this background, the possibilities of simulating ion-solid interactions are discussed, emphasizing effects and literature relevant to the experiments on ion-nanostructure interactions investigated in this thesis.

## 2.1 Ion-solid interactions

### Electronic Energy loss

An energetic ion impinging on a solid will lose its kinetic energy  $E$  to the solid over the distance traveled  $x$  in a variety of processes. The stopping power  $S_e$  is well described for a large energy range by the Bethe (sometimes “Bethe-Bloch”) formula [Bet30, Blo33] derived using the Born approximation perturbation theory on the impact between the ‘fast’ ion and the ‘slow’ electrons in the solid:

$$S = \frac{dE}{dx} = -A \cdot \frac{\rho Z_2 \cdot Z_1^2}{\beta^2} \cdot \left[ \ln\left(\frac{B \cdot \beta^2}{Z_2 \cdot (1 - \beta^2)}\right) - \beta^2 \right], \quad (2.1)$$

with  $A$  and  $B$  positive combinations of constants,  $\rho$  the density and  $Z_2$  the atomic number of the target,  $Z_1$  and  $\beta = v/c$  the atomic number and relativistic velocity of the ion. Corrections to this formula are especially necessary for low ion energies, but in detail they are dependent on the target composition, the ion energy and ion mass in a non-trivial way. Figure 2.1 illustrates stopping regimes and where corrections are required to the Bethe formula. The figure and discussion are adapted from reference [Sig04].

## 2.1 Ion-solid interactions

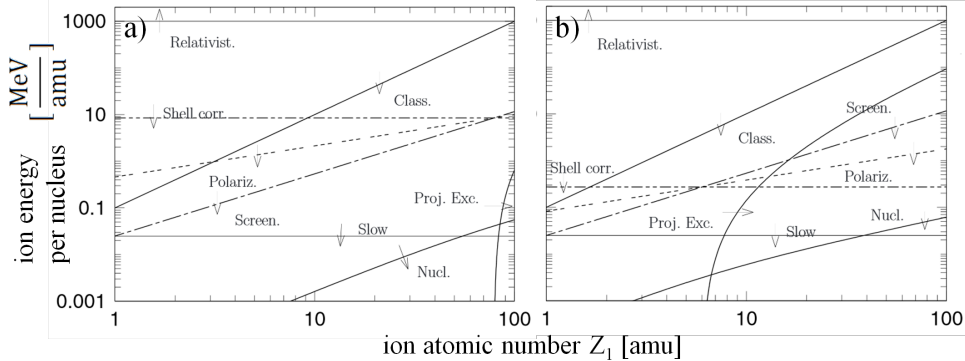


Figure 2.1: Illustration of the dominant effects on the electronic stopping power for an ion of mass  $Z_1$  and energy  $E$  in Au a) and C b). Adapted from [Sig04].

At high ion energies ( $> 1 \text{ GeV}/\text{amu}$ , labeled “Relativist.”) highly relativistic effects have to be taken into account. At these energies we have, for example, the generation of Cherenkov radiation. The horizontal line labeled “Shell corr.” marks the Thomas-Fermi velocity ( $Z_2^{2/3}v_0$ ) of the target electrons, with the Bohr velocity  $v_0 = e^2/\hbar = 25 \text{ keV}/\text{amu}$ . In the parameter-space below this line the ion is moving at speeds comparable to that of electrons in the target, so that a correction for the energy levels (shells) in the target has to be made. In the low energy area below the second horizontal line labeled “Slow” (at  $25 \text{ keV}/\text{amu}$ ) the ion is traveling at speeds below the Bohr velocity of the target electrons. Here, the ion velocity is only comparable to that of the valence electrons in the solid. Now the actual electron density distribution and chemical nature of the solid becomes relevant, which is of course not considered in the general Bethe formula. Therefore, for low ion energies a general and accurate theoretical prediction of the stopping power becomes impossible. Specific ion-target combinations require dedicated investigations.

Above the line showing the Thomas-Fermi velocity of the ion ( $v = Z_1^{2/3}v_0$ , “Screen.”) the ion can be assumed to be stripped of all its electrons. Below, an additional screening function must consider the effective charge of the ion, the theoretical framework for the correction is found in the Lindhard theory [Lin54]. Below the curve labeled “Proj. Ext.” the ion (projectile) carries a comparable number of electrons to the target making excitation processes in the electronic configuration of the ion significant.

## 2 Background

For ion velocities  $v < (Z_1 Z_2)^{1/3} v_0$  (labeled “Polariz.”) a higher order ( $Z_1^3$ ) correction term to the Bethe formula becomes relevant due to the Barkas-Andersen effect. Barkas et al. found that the stopping power was unequal for particles and anti-particles [SBB53]. This leads to a charge-dependent correction term quantified by Andersen et al. [ASS69, SS14]. Below the line marked “Class.” ( $Z_1^2 \cdot 100 \text{ keV/amu}$ ) classical Bohr orbits can be used for electrons around the ion, this is a *sufficient* criterion for the derivation of the Bethe formula not a *necessary* one.

Thus, electronic stopping  $S_e$  is the sum of the interactions between the ion and the electrons in the irradiated solid. In the simplest case a target atom is ionized, followed by a host of effects such as characteristic X-ray emission and Auger electron emission associated with the relaxation of this excited state. Analogously, excitation in a semiconductor is associated with band to band transitions, exciton recombination etc. [Wie88, BFS<sup>+</sup>12]. The luminescent and fluorescent relaxation mechanisms are, however, generally not very efficient. Most of the energy deposited in the electronic system will be turned into kinetic energy of electrons and subsequently converted to phonons/heat. This happens very locally on the *nm* scale of the electrons mean free path and thus also very quickly, within the order of *ps* [TDP92, Nas08].

The effects of such local heating on a solid are diverse. Defects and amorphous regions may either appear or disappear, depending on the material and its history. For large ion masses and energies (swift, heavy ions), the deposited energy density becomes large enough to form an “ion track” around the path of the ion. Swift heavy ion tracks are a whole field of research outlined well by references [TDP92, MK97, WKW04]. Very large electronic losses have to be treated carefully as a large percentage of the electrons within the track are energized and some electrons also gain a significant amount of kinetic energy.

The energies used in this dissertation are in the order of  $\approx 100 \text{ keV}$  with elements of mass  $\approx 100 \text{ amu}$ . The energy regime investigated in this dissertation is thus right at the bottom of the area plotted in figure 2.1. Electronic stopping is not dominant, so that it is sufficient to treat the electronic energy loss as a local heat source.

## 2.1 Ion-solid interactions

### Nuclear energy loss

In the region marked ‘Nucl.’ in figure 2.1, at low ion energies and for heavy ions, the interaction with the electronic system becomes weak. Here, the contribution of the coulomb interaction between ion and individual target atoms as a whole become the main contribution to slowing down the ion. This is called nuclear stopping in contrast to the electronic stopping discussed in the previous section, as kinetic energy is transferred to the target nuclei, not just the electrons. Its first observation was in the famous Rutherford (Geiger–Marsden) experiment [Rut11] which was groundbreaking to the understanding of the structure of matter. Nuclear energy loss arises from the kinetic energy which is transferred from the energetic ion onto an atom in the target. As the impinging ion can transfer considerable energy to an atom, the atom can leave its lattice site and in turn collide with other atoms in the target, leading to the formation of a collision cascade. This displacement of atoms from their lattice position is the main contribution to irradiation damage and sputtering of the target.

The amorphization of crystalline semiconductors has been investigated extensively, a good review is given by reference [WWS12]. The damage production depends strongly on the properties of the irradiated semiconductor and on the density of the collision cascade caused by the irradiating ion. In general, the defects produced by nuclear energy loss are Frenkel pairs. On further irradiation, interstitials and/or vacancies can agglomerate to form extended defect clusters which initiate amorphization. The ion fluence at which the material is amorphized is highly temperature dependent as Frenkel pairs can anneal at elevated implantation temperatures. This can lead to an arbitrarily high amorphization fluence, if the annealing of defects is faster than their creation. A typical ‘radiation hard’ material is  $ZnO$ , which is not amorphous even after  $10^{17} \text{ cm}^{-2}$  of  $200 \text{ keV } Ar^+$  irradiation at  $15 \text{ K}$  [WWS12]. An arbitrarily large amorphization threshold can also be obtained for  $Si$  irradiated with  $300 \text{ keV } Ar^+$  at  $300^\circ C (\approx 600 \text{ K})$  [PMB04].

In addition to the activation of defect recombination by increasing the ‘global’ temperature, an increased local temperature by the energy deposited by the ion will also lead to ‘dynamic annealing’ [Dha07]. The reduction of structure sizes leads to larger dynamic annealing as there is less material into

## 2 Background

which the energy deposited by the ion can dissipate, leading to higher local temperatures. This was shown in the *Mn* irradiation of *GaAs* nanowires [Bor12, JHMR15] and was used to improve the magnetic properties of the *GaAs:Mn* nanowires [BMB<sup>+</sup>11, PKB<sup>+</sup>12, KPJ<sup>+</sup>13, PKJ<sup>+</sup>14].

### The binary collision approximation

A typical assumption in the theoretical treatment of nuclear energy loss is the binary collision approximation (BCA) for the ion and the target atoms [Eck91]. Under this assumption nuclear stopping is treated as a series of collisions between single particles. With the additional assumptions of 1) a spherically symmetric interaction potential and 2) the neglect of possible electronic effects (chemical binding) between the collision partners, the angular-momentum is conserved in the collision and the classical scattering-integrals can be solved [ZLB85].

As an example, the resulting trajectories of a *Si-Si* collision at 10 eV is plotted in figure 2.2. The large difference between the Moli  re screened Coulomb potential [Mol47] and the “*Si-Si*” potential [HFH<sup>+</sup>90], derived by Dirac-Fock-Slater calculations, is clearly visible. The former is a purely repulsive Coulomb interaction, while the latter includes an attractive interaction for large interatomic distances similar to the well known Lennard-Jones potential [Jon24, Eck91]. For high energy collisions a “universal” Ziegler-Biersack-Littmark (ZBL) potential based on a screened Coulomb interaction is quite successful [ZLB85], however for low energy collisions a generalized formula cannot be accurate and specific potentials have to be developed for each combination of collision partners [Ded95, NRS97, ANNKO02, ND08].

In addition to this problem of finding the correct interaction potential for a collision, depending on the ion and the atomic structure of the irradiated material, the collision parameters relevant to low energy collisions are within the order of the inter-atomic distance of a few Å, as shown in figure 2.2. The assumption that this is still a binary collisions can no longer be valid. In conclusion, it has to be noted that similar to the electronic stopping case, the assumptions for a generalized treatment of nuclear stopping are well fulfilled for large ion energies, but lose their validity at low energies  $\ll 1 \text{ keV}$ .

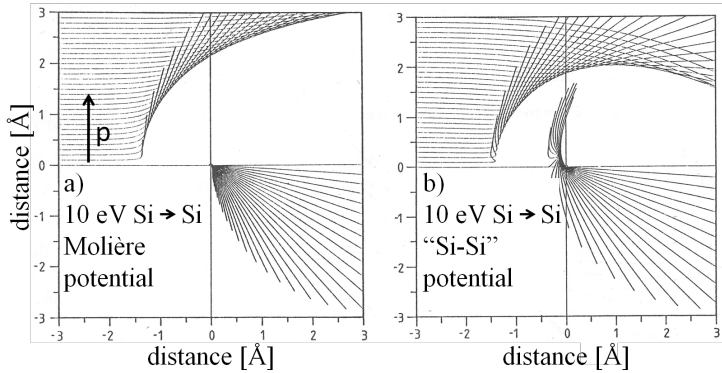


Figure 2.2: Trajectories of a 10 eV  $Si-Si$  collision for a) Moli  re and b) “ $Si-Si$ ” potential. The trajectories end after the same elapsed time for each impact parameter  $p$ . Adapted from [Eck91].

### Sigmund theory of sputtering

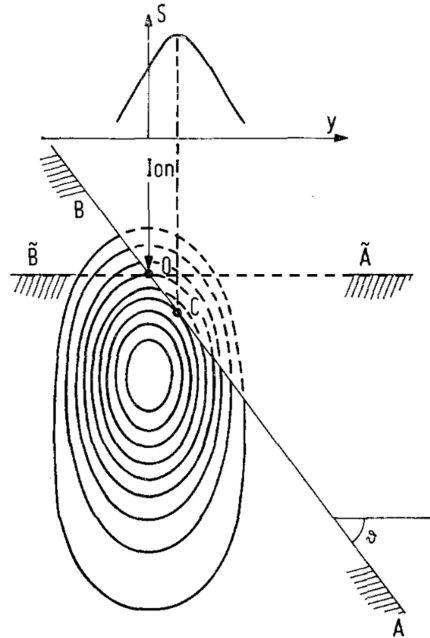
A prominent role in this dissertation will be played by a special effect of nuclear energy loss arising when the path of a recoiled atom intersects the targets surface: sputtering. The foundation of a sputter theory was laid by Sigmund [Sig69]. The nuclear stopping of ions leads to the formation of highly branched collision cascades and most of the recoiled atoms are found at the end of the many branches. Because of this, the majority of sputtered particles has a low energy and thus a low range in the material [Tho68]. Therefore, predominantly atoms close to the surface of the target contribute to the sputter yield. The number of atoms sputtered per impinging ion can be estimated by calculating the nuclear energy loss at the surface of the irradiated material, divided by a factor to account for the probability of an atom leaving the solid. The probability for the atom to leave the solid includes geometric considerations and the ‘surface binding energy’ (SBE). A possible model for an atom leaving a solid is that of a potential plateau with the height of the enthalpy of sublimation, which has to be overcome by the atom approaching the surface. This equates the energy required for sputtering an atom to the thermal energy required for sublimation. For metals this is a good assumption, as the metallic bond is undirected and mediated by the electron gas. However, the SBE model for sputtering neglects all effects related to the directionality of the local binding forces experienced by the atom to be sputtered and the mod-

## 2 Background

ification of the surface by repeated removal of atoms, which will be relevant in compounds with covalent or ionic bonds.

A reasonable assumption for the mean nuclear energy deposition distribution is a Gaussian ellipsoid, with the center at the ion range and the longitudinal and lateral straggling naturally defining its extensions. This approach was used by Sigmund to arrive at a good explanation for the energy dependence of sputtering from flat surfaces [Sig69]. Starting at low ion energies, the sputter yield will initially increase with increasing energy, simply due to more energy being available. For further increasing ion energy, however, the ion range becomes larger, leading to a predominant deposition of the energy deeper inside the target, away from the surface. A maximum is thus found at ion energies where the ion range is in the order of the longitudinal straggling. The angle dependence of sputtering can also be explained by the increased deposition of energy near the surface for larger angles of incidence, as shown in figure 2.3.

Figure 2.3: Illustration of the Sigmund model of sputtering for irradiation of a bulk sample at an angle  $\theta$ . The ion enters the target at the point O and deposits energy by nuclear stopping as indicated by the oval contours. The energy deposited along the inclined surface BA is larger than that for the perpendicular surface  $\tilde{B}\tilde{A}$  leading to increased sputtering for irradiation at an angle. Also the deposited energy and thus sputtering is not largest exactly at the point of incidence O, but further down at the point C. This is illustrated by the projection of the sputter yield ‘S’ onto the lateral dimension ‘y’. Adapted from [Sig73].



With the situation illustrated in figure 2.3, the Sigmund theory can explain surface roughening by ion bombardment. For example, the Bradley-Harper theory of ripple formation on ion irradiated planes relies on the anisotropic sputtering predicted by the Sigmund model applied to a structured surface

## 2.2 Simulation of ion-solid interaction

[Sig73, BH88]. The increased sputtering at a point (C), downstream from the point where the ion enters the target (O), leads to an enhancement of surface roughness.

The Sigmund theory can also be applied to curved surfaces. For nano-sized spheres or cylinders, the Sigmund theory can be invoked to predict that the sputter yield will be maximum when the ion range is comparable to the nanostructure diameter. Consider sputtering for a fixed ion energy and a varying diameter, illustrated in figure 2.4. At extremely large diameters atoms can only be sputtered from the flat surface (A in figure 2.4) facing the ion beam. The sputter yield will still be larger than for an unstructured bulk sample as the local angle of irradiation is increased for non central impacts. For decreasing diameters the curvature of the nanostructure increases, further increasing the intersection area between the estimated energy distribution and the nanostructure (B in figure 2.4). Once the diameter is in the order of the ion range, ‘forward’ sputtering along the direction of the ions initial path becomes possible (C in figure 2.4). There is a maximum sputter yield for a radius comparable to the ion range, because the total surface area shrinks as  $1/r^2$ , reducing the sputter yield again for decreasing diameters.

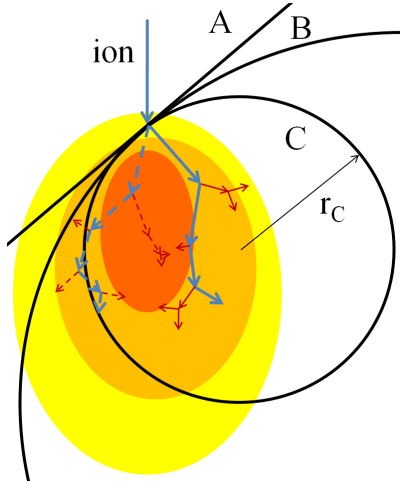
This model is obviously limited, as the energy distribution is assumed to remain constant even if it is intersected by the target surface (dashed lines in figure 2.3). The maximum in the Gaussian ellipsoid approximation of the mean energy deposition is found where many of the branches of collision cascades overlap. A constant distribution wrongly includes those ion paths that would have left the nanostructure, as shown by the dashed ion trajectory in figure 2.4. Thus, a more detailed description of the process is required.

## 2.2 Simulation of ion-solid interaction

In practice, the theory of ion-solid interactions is implemented in simulation tools, which allow the experimenter to predict experimental outcomes. Most frequently the energy dependence of the ion range is obtained by such simulations and used to decide which ion energy and ion fluence of irradiation is needed to create a desired doping concentration profile. On a more fundamental level, an experimentally observed behavior can be understood better by comparing it to various simulations to discern the dominating effects. The

## 2 Background

Figure 2.4: Illustration of the Sigmund model of sputtering for irradiation of a curved surface. For an infinite curvature radius (straight line A) a non-central impact is the same as irradiation at an angle, as shown in figure 2.3. For decreasing radii (B) the intersection between the colored energy distribution and the surface is increased. For small radii ( $r_C$ , C) forward sputtering appears. Two exemplary ion paths contributing to the colored average energy distribution are shown. The dashed path leaves and returns to the the smallest structure C.



two main simulation approaches used for the ion-solid interactions are Monte-Carlo (MC) and molecular dynamic simulations (MD), both outlined in the following sections. Two dated, but highly recommendable reviews on the topic are given in references [And86, Eck91].

### Monte-Carlo simulations

Monte-Carlo codes are simulation codes that use random numbers for simulations. After numerous simulations with different randomized outcomes, a statistical approximation of the likely outcome can be derived. With the BCA, the solid ion-interaction lends itself very well to MC simulation, as the evolution of a collision cascade can be simulated by following the paths of the ion and all recoils reiteratively from one collision event to the next. The probability of a collision can be determined from the cross-sections determined by the interaction potential between the projectile and the atoms in the target. According to this probability, a randomized distance traveled in a straight line by the projectile is determined. The particle's kinetic energy is reduced by the electronic energy loss accordingly. This has the underlying assumption of a ‘random material’ and crystal structure effects such as channeling are not reproduced by such a simulation. Two further random numbers are used to determine the impact parameter and azimuthal angle. The trajectories of the projectile and target atom in the plane of impact after the impact are deter-

## 2.2 Simulation of ion-solid interaction

mined by this impact parameter, the interaction potential and the particle energy, as shown in figure 2.2.

Examples of simulation codes implementing this approach in planar targets are TRIDYN [ME84], SDTrimSP [BMS<sup>+</sup>08], corteo [Sch08], COSIPO [Hau84] and, by far the most popular, SRIM [Zie12]. The target composition is treated dynamically in TRIDYN and SDTrimSP, changing with the incorporation of ions and with selective sputtering of target atoms and the incorporated ions. It is clear from the discussion of chapter 2.1 and figure 2.4 that the irradiation of a nanostructure can not be approximated well with a planar simulation. Therefore, the recently developed TRI3DYN [Mö14] and *iradina* [BR11] run a BCA MC simulation in a volume subdivided into rectangular voxels containing either vacuum or material to represent a three dimensional, structured target. TRI3DYN even includes dynamic composition and structural relaxation during the irradiation on a three dimensional simulation volume, but unfortunately it is not publicly available yet. Several *iradina* simulation results will be discussed in this thesis, so some points on the expected accuracy have to be made.

The advantage of MC BCA simulations in general is that the direct simulation of the ion trajectories gives an accurate prediction of the final distribution of the ions in the target. This is a result of the sufficient accuracy of the previously discussed underlying theory of the energy losses for high ion energies. These predominantly determine the distance traveled by the ion in a collision cascade and also the distribution of nuclear and electronic energy loss. As the simulation directly follows the ions path, this accuracy can be expected to be upheld in the irradiation of nanostructures, such as nanowires. The concentration of incorporated ions is somewhat lower in nanowires than in bulk targets, as in a nanowire there are more possible paths that lead to the ions being scattered out of the nanowire, than there are in the irradiation of a bulk surface, see chapter 2.1, figure 2.4 and reference [Bor12].

Predicting the damage caused in the material by nuclear energy loss is a much more difficult prospect. The *iradina* code checks at each collision whether the target atom acquires more energy than the “displacement energy” which is a material specific parameter. If an atom has less than the displacement energy after a collision, it is assumed to remain bound in its place and the energy is converted into phonons. Atoms with more energy

## 2 Background

are displaced, creating a Frenkel pair which is counted as an interstitial at the location where the atom finally comes to rest and a vacancy at its point of origin. The displacement energy is experimentally accessible for crystalline materials by electron irradiation experiments in which the irradiating electron energy is in the order of  $MeV$  [CW65]. From the electrons' impulse and mass the maximum transferred energy can be calculated. The defects produced as a function of electron energy can thus be used to determine a threshold energy transfer for the creation of point defects, and this value is defined as the displacement energy. This is not possible for amorphous materials, where point defects are ill-defined. Also, the number of Frenkel pairs is only an estimation at the *creation rate* of the defects. The critical role that defect mobility, agglomeration and annealing plays in ion irradiation, especially at elevated temperatures, is totally neglected [PMB04, Nor14].

Better results can be expected for the computation of sputtering by MC simulation tools, for which an excellent review is given in reference [Bie87]. The difficulty is that for low projectile energies the interaction with both the nuclear and the electronic system are not generalizable, as discussed in chapter 2.1. This is a problem, as the dominating contribution to sputtering is made by low energy recoils [Tho68]. The various relevant interaction potentials, however, differ most at low energies. In addition, the SBE model used for Sigmund sputtering is just an approximation of the complexities arising at real surfaces. For metals the situation is most favorable and in reference [Bie87] sputter yields of various metals are reproduced quantitatively. More recently, in reference [HZM14] by Hofsäss et al., good results on the sputtering of *Si* and *Ge* were obtained using the *Kr-C* [WLB77] potential which was found to be superior to the ZBL potential [ZLB85]. In *iradina* only the ZBL potential is implemented, however, neither the *Kr-C* nor the ZBL potential reproduce the angle-dependent potential of covalently bonded solids such as *Si* [SW85, Ter88]. Radially symmetric potentials are always only an approximation and which potential provides the better approximation in which scenario is not generally clear.

Hofsäss et al. [HZM14] also report a change in the dependence of sputtering on the angle of incidence for different interaction potentials. This might be worrisome even for the qualitative dependencies in the irradiation of nano-structures investigated in this thesis. However, the effect of different potentials

## 2.2 Simulation of ion-solid interaction

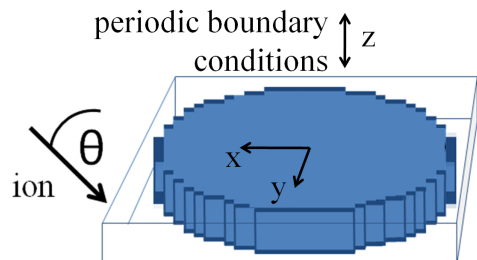
on angle-dependent sputtering is caused by the change in the critical angle for scattering at the surface of the impinging ion, not by a later change in the distribution of the nuclear energy deposition within the target [EHHF92]. Since the critical grazing incidence angle is close to  $0^\circ$  regardless of the interaction potential for the relatively high energies ( $\approx 100\text{ keV}$ ) used in this dissertation [YS84], the accuracy of qualitative predictions will be unaffected. Finally, Hofsäss et al. [HZM14] also compared reported experiments on the compounds  $Ta_2O_5$  and  $SiO_2$  with simulations, finding that composition changes, caused by preferential sputtering of one element in the compound, play a significant role. This makes dynamic simulations necessary. As this is not possible in *iradina*, it will be discussed where relevant.

Even though *iradina* can implement an analytical description of a cylinder [Bor12], most of the simulations in this work were performed on the voxel based simulation volume, as this granted more freedom in the creation of the simulation volumes. A typical simulation volume is shown in figure 2.5. The number of target atoms leaving the simulation volume per impinging ion gives the sputter yield. To ensure *iradina* accounts for the surface binding energy correctly, the outermost voxel of the simulation volume has to contain vacuum, so that a sputtered atom makes a material-to-vacuum transition inside the simulation volume. Where the axial distribution was not relevant, the voxel  $z$ -size was set to  $10\text{ nm}$  with periodic boundary conditions. The accuracy of the approximation of a curved surface in the  $xy$  direction, such as the surface of the cylindrical nanowires, is obviously dependent on the voxel size. Since the surface of the approximation by rectangular voxels of a cylinder is strictly larger than the analytical surface, sputtering may be slightly increased. Also, the possible ions' impact angles are limited to the angle between the ion beam and the plane surfaces of the voxels facing the ion beam, so that the impinging angle is always larger in the voxelated surface than for the analytical surface. However, this will have no large effect, since, as before, the small critical angles for reflection of ions are restricted to the very outermost edges of the nanowire. Considering these effects, it was found that for voxel edges of  $2\text{ nm}$  and below only a negligible influence of the voxel size on the sputtering remained.

In summary, the prediction of sputtering as simulated by *iradina* in this thesis is expected to be dependable with respect to the qualitative relationship

## 2 Background

Figure 2.5: Typical implementation of a nanowire for an *iradina* simulation. The ions enter the simulation volume at  $x = 0$ ;  $y, z = \text{random}$  with an angle to the  $z$ -axis of  $\theta = 45^\circ$ . The  $x$  and  $y$  direction have 102 voxels of  $0.02 - 2 \text{ nm}$  edge-length so that nanowire with diameters of  $2 - 200 \text{ nm}$  can be simulated. The  $z$ -direction is periodically continued.



between ion range and structure size, and sputtering. Quantitative sputter yields will, however, be inaccurate.

### Molecular dynamic simulations

The MC BCA simulations outlined so far inherently neglect all effects occurring when more than two particles move at the same time. Molecular dynamic (MD) simulations, however, follow the path of every particle in the simulation volume individually, calculating the interaction potential between them at every time step [AW59]. Obviously this is much more computationally expensive than the BCA and simulation volumes and times are thus limited. Nevertheless, the method can be applied to ion irradiation [Nor95] and increasing computer power has led to the simulation of ever higher particle energies, which require a larger simulation volume and time [GHB<sup>+</sup>13, BD14, ABU15]. The interactions between the target atoms in the MD simulations have to recreate the atomic structure, thermal vibrations etc., so that the low energy regime of the interaction potential is critical and has to be adapted to the specific problem [Ded95, NRS97, ANNK02, ND08]. Electronic energy loss can be included as a frictional force, however, treating this energy in a consistent manner is a problem, as the electronic system is typically not explicitly represented. Since MD simulations can reproduce the thermal evolution of a system, references to relevant MD simulation studies will be included in the discussion of results in this thesis.

## *2.2 Simulation of ion-solid interaction*

### **Relevant simulations in literature**

Two recent investigations on sputtering of spherical [NSUM14] and cylindrical [UBNM15] nanostructures have to be mentioned here as they overlap significantly with the studies made in this thesis. These publications have found the Sigmund model, as it was discussed in chapter 2.1, to be a decent first approximation for sputtering of nanostructures. They go on to compare the sputter yield results from MC and MD simulations and discuss its diameter dependence. Unfortunately, the nanowire diameters investigated by MD are quite small owing to the computational costs. They find that for decreasing nanostructure diameters sputtering of clusters and thermal evaporation become increasingly important due to the lower number of atoms amongst which the ion deposited energy is distributed. This dissertation adds to results of these studies with explicit simulations of diameter and energy-dependent sputtering of nanowires in chapter ?? and an experimental investigation of this dependency in the following chapter ??.

# 3 Experimental Methods

## 3.1 Nanowire synthesis

Nanowire synthesis can be categorized according to two approaches: “bottom-up” and “top-down”. The “bottom-up” approach relies on the self-organized arrangement of matter using an inherent anisotropy in the growth mechanism to create nanoscale structures. Depending on the material, crystal quality, morphology, infrastructural requirements, the quantity to be produced etc. there is a large variety of processes available for synthesis. The *ZnO* [BMS<sup>+06</sup>, Sti08, Mü09, CZC<sup>+10</sup>, Ogr13] and *Si* [LSH<sup>+08</sup>] nanowires investigated in this dissertation were grown using vapor transport, pulsed laser deposition (PLD) and chemical vapor deposition (CVD) respectively.

A very common mechanism to create the anisotropy required to get the one dimensional growth of nanowires is the vapor-liquid-solid growth (VLS) first described by Wagner and Ellis [WE64]. The growth of the “bottom-up” nanowires used in this thesis relies on the VLS mechanism. The variety of processes available for nanowire growth are responsible to provide the ‘vapor’ of material for this growth mechanism. With the vapor transport technique the source material eg. *ZnO* is simply evaporated in a typically inert atmosphere and transported within a reactor to the substrate by diffusion or gas flow. Chemical vapor deposition uses reactive gases such as *SiH<sub>4</sub>* to provide the source material, in this case *Si* in a temperature and pressure controlled reactor.

Although self-catalyzed growth has also been observed, the liquid phase exploited in VLS is typically provided by a metal catalyst deposited on the growth substrate [DL00, WDJ<sup>+09</sup>]. The material in the vapor phase can accumulate in the catalyst droplet until the concentration is supersaturated. Preferential segregation of the excess material at the droplet-substrate interface leads to the growth of a nanowire. The size of the droplet can be used

### 3.1 Nanowire synthesis

to control the diameter of the grown nanowire to some extent. An epitaxial relation between the substrate and the nanowire material may be used to direct the growth. Typical nanowire diameters and lengths are  $50 - 300\text{ nm}$  and  $> 5\text{ }\mu\text{m}$  respectively.

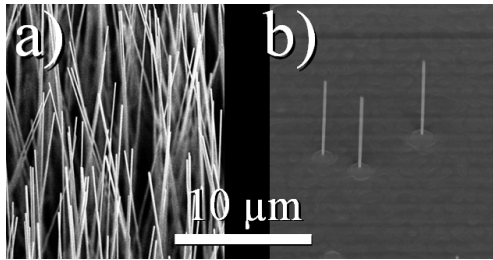


Figure 3.1: SEM images of the  $ZnO$  nanowire samples. In a) the dense samples grown via vapor transport on AZO are shown, while b) shows the sparser, PLD grown  $ZnO$  nanowires on a sapphire substrate.

Relatively dense  $ZnO$  nanowire samples are grown by vapor transport in Jena in the three-zone-furnace (3ZJ). The nanowires grow upstanding on a  $\approx 500\text{ nm}$  layer of  $Al$  doped  $ZnO$  (AZO) sputtered onto a  $Si$  substrate, as shown in figure 3.1a. The temperature at the 1 : 1 molar source mixture of  $ZnO$  and  $C$  was  $1050\text{ }C^\circ$ , the substrate position at  $46\text{ cm}$ ,  $Ar$  and  $O_2$  flow  $10\text{ sccm}$  each and the base pressure  $7\text{ mbar}$  [BMS<sup>+</sup>06, Sti08, Mü09, Ogr13]. Further  $ZnO$  nanowire samples with a sparser lateral distribution of the upright nanowires on a sapphire substrate decorated with  $Au$  colloids are shown in figure 3.1b. They were kindly provided from the University of Leipzig by Dr. Helena Franke. The parameters for the PLD growth of these samples are a laser power density of  $2\text{ J/cm}^2$ ,  $165\text{ mbar}$  base pressure at  $40\text{ sccm}$   $Ar$  flow, a substrate temperature of  $900\text{ }C^\circ$  and a target-substrate distance of  $35\text{ mm}$  [CZC<sup>+</sup>10].

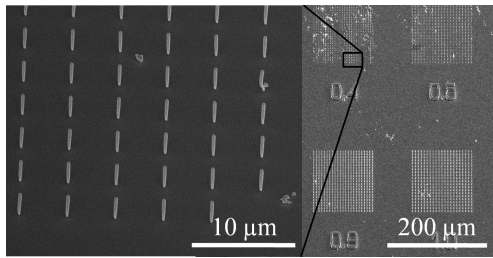


Figure 3.2: SEM images of the etched  $Si$  nanowire arrays. On the right, the numbers etched into the substrate under each array indicate the diameter in  $\mu\text{m}$  of the predefined  $Ni$  mask for that array.

Nanowires can also be synthesized “top-down” [HIK97, HKZ<sup>+</sup>10]. A “top-down” approach requires a predefined template which is used to control the desired morphology. The  $Si$ -nanowire arrays used to study sputtering and plastic deformation within this dissertation were etched by reactive ion etching (RIE) through a circular, e-beam lithographically defined  $Ni$  hard-mask

### 3 Experimental Methods

which set the nanowire diameter [JNW<sup>+</sup>15]. The RIE parameters were a flow of  $50\text{ sccm }SF_6$  and  $100\text{ sccm }O_2$  at a set pressure of  $10\text{ mTorr}$  and a strike pressure of  $30\text{ mTorr}$ . The radio frequency and inductive coupled plasma powers were  $15\text{ W}$  and  $100\text{ W}$ , respectively. The etching was performed at  $-108\text{ C}^\circ$  for  $5\text{--}15\text{ min}$ . After the RIE process, a  $32\%$   $HCl$  and (7:1)-buffered  $HF$  dip removed the *Ni*-hard mask and the oxide formed at the surface of the *Si*, respectively. Using this “top-down” etching process it is possible to prepare nanowires with diameters varying from  $50\text{ nm}$  to  $2\mu\text{m}$  with a height of  $\approx 3\mu\text{m}$  on a single substrate for simultaneous irradiation. As seen in figure 3.2, the spacing between the nanowires was larger than their height, so that there is no shadowing of the ion beam between the nanowires.

## 3.2 Modification

### ROMEO

The ion irradiation for this dissertation was performed at the general purpose High Voltage Engineering implanter “ROMEO” at the IFK in Jena. It can provide an ion beam of virtually any element at energies ranging from  $10\text{ -- }380\text{ keV}$ . The beam passes a  $90^\circ$  selector magnet and can be swept with a frequency of  $\approx 1\text{ kHz}$  to homogeneously irradiate areas up to several tens of  $\text{cm}^2$  with ion currents of up to  $1\text{ mA}$ . For this work ion current densities were limited to  $500\text{ nA/cm}^2$ , corresponding to  $\approx 15\text{ min}$  for the typical fluence of  $10^{16}\text{ ions/cm}^2$ .

Previous work has shown that nanowires can bend under ion irradiation [BSL<sup>+</sup>11, Bor12]. Therefore, a rotatable, heatable and tilted stage (RHT), illustrated in figure 3.3, was custom built within the frame of this thesis, together with Stefan Noack [Noa14]. With it, bending of the upstanding nanowires can be avoided as the nanowires are irradiated homogeneously from all sides at an angle of  $45^\circ$ . All the samples investigated in this thesis were rotated on the RHT and its preceding prototype sample stages during the irradiation.

The sputtering and plastic deformation studies in chapters ?? and ?? were conducted with  $Ar^+$  irradiation in *Si* nanowires to avoid any chemical effects of the incorporated ions. To prevent defect induced density changes and

### 3.2 Modification

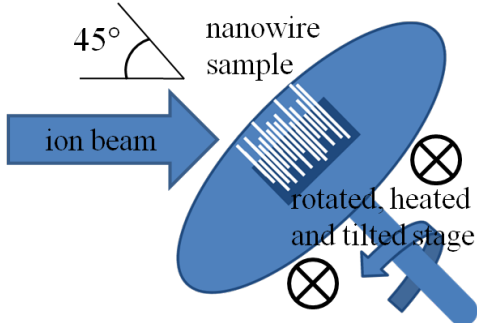


Figure 3.3: *RHT Foto* Illustration of the rotated, heated and tilted (RHT) stage for the ROMEO implanter. The rotating stage is tilted towards the ion beam by 45° and heated from the back by two light bulbs. The temperature is controlled by a reference measurement on a stationary disk similar to the rotating stage.

the *Si* nanowires from amorphizing, the irradiation temperature was 300° for the sputtering study. At this temperature the amorphization threshold becomes arbitrarily high [PMB04]. The other irradiations were performed at room-temperature. For the quantification of dopants in chapter 4, *ZnO*-nanowires were irradiated with  $Mn^+$ .  $Mn$  has a similar mass to  $Zn$  and both are medium-weight so that the linear cascade theory is applicable. Also,  $ZnO : Mn$  is interesting as a possible material for diluted magnetic semiconductors (DMS) [Fur88, NKA<sup>+</sup>04]. Pragmatically, it is relatively easy to get a stable  $Mn^+$  beam with ROMEO and with the quantification in mind,  $Mn$  is much less likely to be in any components at the XRF beamline and give a background than *Fe, Co, Ni* or *Cu*.

### Focused ion beam - FIB

Some sample preparations required a FIB. These are highly specialized ion accelerators with the main objective of obtaining a small ion beam focus. Most of the systems use a  $Ga^+$  beam and acceleration voltages up to 30 keV. The main use for FIBs is to sputter material extremely locally, making it a versatile tool for nano-machining. The FEI DualBeam Helios NanoLab 600i FIB system used for this dissertation is a scanning electron microscope (SEM) - FIB combination. The sample can thus be milled with the ion beam and investigated with the SEM reiteratively. The system is also equipped with a *Pt*-metal-organic gas injection system. The *Pt* containing organic molecule can be cracked locally on the sample by the secondary electrons created by either the electron or ion beam. Most of the *Pt* is deposited near the impact point of the primary beam at the substrate. However, typically a rather

### 3 Experimental Methods

large ‘halo’ of minor *Pt* deposition can extend for a couple of  $\mu m$ . The FIB system can thus mill and deposit structures on a  $nm$  scale. For the sample preparation in this thesis all *Pt* deposition was done with the electron beam to avoid damage to the nanowire by the  $Ga^+$  ion beam.

## 3.3 Characterization

### Scanning Electron Microscope - SEM

The morphological changes in the nanowires were characterized by high resolution SEM in the FEI DualBeam Helios NanoLab 600i FIB system. The lateral resolution of the SEM system is  $\approx 2 nm$ . Images of individual nanowires were made before and after ion irradiation to quantify the sputtering. To find exactly the same place on the sample, a series of images with increasing magnification has to be made. Typically, images were made at an angle of  $45^\circ$  to the substrate with the alignment procedure the same before and after irradiation.

A semi-automated image analysis protocol was developed by Stefan Noack in his Master thesis [Noa14, JNW<sup>+</sup>15] to evaluate the SEM images of a large number of nanowires. It applies a (3x3) median filter to smooth out some noise and a Gaussian unsharp mask with  $\sigma = 1 px$  and weighted at 60 % to resharpen the edges [San04]. An Otsu threshold [Ots79] is applied to separate the brighter nanowire from the darker background. Next, open source particle analysis software is used to find the main body of the nanowire and turn it upright, correcting any marginal tilt remaining in the SEM images [SACF<sup>+</sup>12, SPTS12]. Finally the sum of the gray-values in each line is used to calculate the diameter at that height along the nanowire axis. As the investigated nanowires showed a characteristic bulge at the base, this point was used to align the height profiles of a single wire before and after irradiation. To avoid any irregular effects by the altered geometry at the top facet and the base of the nanowire,  $\approx 20\%$  of the height was disregarded at either end of the extracted profile. After a fluence of  $10^{16} cm^{-2}$  the change in diameter was close to the resolution limit of the SEM, therefore only the data for two subsequent irradiation steps of  $2 \cdot 10^{16} cm^{-2}$  ions was evaluated. A more

### 3.3 Characterization

detailed description of the image analysis process can be found in reference [Noa14] and the supplementary information of reference [JNW<sup>+</sup>15].

#### **Electron Back-Scatter Diffraction - EBSD**

A Carl Zeiss Auriga CrossBeam Workstation fitted with an EBSD tool was used to identify whether nanowires remained crystalline after irradiation. The electron beam is focused on the sample at an arbitrary angle and the scattered electrons are detected by a large CCD detector in the SEM. Bragg diffraction along the crystal lattice planes produces a characteristic pattern of Kikuchi lines on the detector [Kik28, FH13] in crystalline samples. Amorphous or nano-crystalline samples show no pattern.

#### **nano-XRF**

Hard X-ray radiation stimulates the atoms within the radiated material to emit characteristic X-ray radiation. This X-ray fluorescence can be detected in an energy dispersive semiconductor detector and used to identify and quantify the elements in the sample [GS28]. In principle the method is similar to the more wide-spread energy dispersive X-ray spectroscopy (EDX), where an electron beam is used to excite characteristic X-ray fluorescence [JS82]. Very good lateral resolution can be obtained by having an EDX detector in a SEM. However, the advantage of using X-rays lies in the absence of Bremsstrahlung which high energy electrons produce in matter in addition to characteristic X-rays. In XRF there is thus a much lower background and much lower concentrations of elements can be detected and quantified. Unlike normal X-ray tubes, synchrotron radiation is very brilliant, allowing it to be focused.

X-ray fluorescence with a nano-focussed X-ray beam (nano-XRF) was measured at the European Synchrotron Radiation Facility (ESRF), beamlines ID16b and ID13. The beamlines were run at various photon energies above  $15\text{ keV}$  and with focal spot of typically  $\approx 80\text{ nm}$  and  $\approx 250\text{ nm}$  diameter, respectively. The nano-XRF thus allows the quantification of low concentrations with sufficient lateral resolution to resolve axial concentration gradients in a nanowire. Unfortunately, the resolution is not high enough to investigate radial distributions.

### *3 Experimental Methods*

For this thesis, *Mn* irradiated *ZnO* nanowires were deposited on TEM grids either randomly by ‘imprinting’ or individually by using the micro-manipulator in the FEI DualBeam FIB. Transferring individual wires requires some finesse, but it is possible to detach *ZnO* nanowires from their substrate without the  $Ga^+$  FIB and to place them on the “lacey-carbon” TEM grids without any additional *Pt* deposition. In this way SEM images before and after irradiation of the same wire investigated by nano-XRF are available. At both beamlines the nanowires on the TEM grids are scanned under the fixed focal point of the X-ray beam with piezo-motors while the XRF spectra are collected with a Vortex EM silicon drift X-ray detector.

The spectra used for quantification were obtained in multiple scans across a nanowire at regular intervals along its length. As the XRF signal can be used to locate the nanowire, only the points near the nanowire were measured with a high integration time and a low step-with ( $< 1/2$  focal spot) to ensure a large number of counts ( $> 10^5$  per scan) at reasonable measuring times.

### 3.3 Characterization

#### nano-XRF quantification

The XRF-Spectra were evaluated using the open source PyMCA software package [SPC<sup>+</sup>07]. The effects of self absorption and excitation can be neglected, as the investigated nanowires are very thin compared to the X-ray absorption length, which is a couple of  $\mu m$  in  $ZnO$ . However, the detector-sample distance is responsible for an unavoidable attenuation length in air. Here, the X-ray absorption is dominated by  $Ar$ . As  $Mn$  is relatively light, its characteristic X-ray emission at  $K_{\alpha,Mn} = 5.9 \text{ keV}$  is absorbed more than the signal of the heavier  $Zn$  with  $K_{\alpha,Zn} = 8.6 \text{ keV}$ . Thus, absorption of the XRF signal in air has to be considered carefully in the fitting with PyMCA. The accuracy was double checked by measuring and quantifying trace elements in a calibration sample of bovine liver. In this way, optimal fitting parameters were found for each beam-time and applied to the respective spectra in the PyMCA batch mode.

Oxygen cannot be quantified in these beamlines, as its XRF emission is totally attenuated by air and a  $Si$  dead layer in the detector. The quantification of the  $Mn$  content in the  $ZnO$  nanowires thus relies on the assessment of the  $Mn/Zn$  ratio. In any case, it is a decent approximation to assume that the  $ZnO$  remains stoichiometric even during the irradiation. The samples are irradiated in a chamber with a base pressure  $\approx 10^{-6} \text{ mbar}$ , so according to the Hertz-Knudsen equation *Cite* this will give a coverage of roughly one mono-layer or  $10^{15} \text{ particles/cm}^2 s$ , if one assumes a sticking coefficient near 1. The maximum ion current density yields  $10^{13} \text{ ions/cm}^2 s$ , so that an unlikely amount of preferential sputtering would be required to deplete the oxygen out of the wires. In addition, the wires will be oxidized in the normal atmosphere post irradiation. The  $Mn/Zn$  ratio is thus a good proxy for the  $Mn$  concentration.

The quantification limit can be estimated using a simulated XRF spectrum from PyMCA. By finding an appropriate photon flux and nanowire interaction volume, the simulation can reproduce the XRF spectrum with the actually measured number of counts at  $K_{\alpha,Zn}$ . The  $Mn$  content in the simulated matrix can then be decreased until the minimum  $Mn$  content is found which gives a signal at  $K_{\alpha,Mn}$  just above the actually measured noise level. In this

### *3 Experimental Methods*

way a lower limit for the concentration resolution can be found at typically 0.1 %  $Mn/Zn$ .

# 4 High Doping Concentrations in Nanowires

This chapter will discuss the concentration of dopants incorporated into ion irradiated nanowires. The simulations and experiments presented in this chapter were all performed with  $175\text{ keV }Mn^+$  irradiated  $ZnO$  nanowires, however, the effects can be easily applied to other material combinations. Some of the results presented in this chapter are also published in reference [JNP<sup>+</sup>14].

## 4.1 Doping and Sputtering

With *iradiana* the distribution of the places where the ions come to rest gives the profile of the concentration of dopants per fluence. Locally the concentration [ $\text{atoms}/\text{cm}^3$ ] increases a certain amount per fluence [ $\text{ions}/\text{cm}^2$ ], leading to the somewhat awkward unit of for the doping efficacy [ $(\text{atoms}/\text{cm}^3)/(\text{ions}/\text{cm}^2)$ ]. An example of the dopant distribution simulated with *iradiana* is shown in figure 4.1a for the irradiation of a  $ZnO$  nanowire with  $175\text{ keV }Mn^+$ . The ions enter the  $y$ - $z$  plane at random locations and at an angle of  $45^\circ$  to the  $z$ -axis, which is periodically continued outside the plane of the image. It is clear that a homogeneous doping profile is not easy to obtain for the irradiation of a nanowire from one side. As with the creation of a box profile in bulk irradiations, multiple irradiation steps with varying energies are required. Note that an ion energy of  $175\text{ keV}$  is obviously not enough to permeate the whole nanowire diameter of  $200\text{ nm}$ , so that an additional irradiation with higher ion energy would be required to obtain homogeneous doping. Rotating the nanowire under the ion beam is a much easier way of increasing the homogeneity of the doping profile. Figure 4.1b shows the local dopant incorporation efficacy for

#### 4 High Doping Concentrations in Nanowires

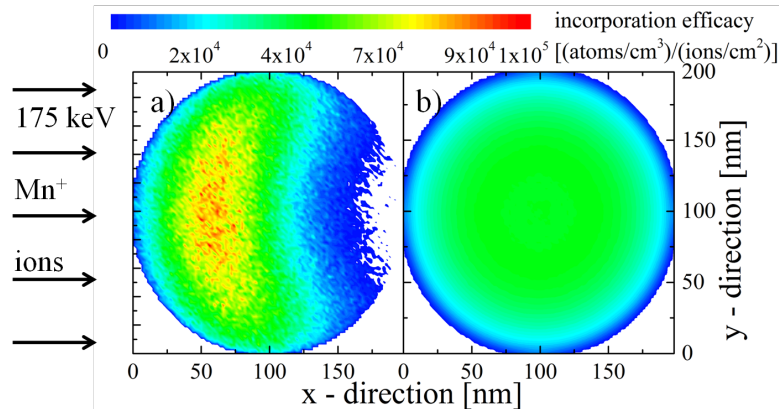


Figure 4.1: a) Color plot of the increase in concentration per fluence for the irradiation of a  $ZnO$  nanowire with  $175\text{ keV}$   $Mn^+$  ions at an angle of  $45^\circ$  to the  $z$ -axis. The energy was selected so that the rotation of this profile produces a radially homogeneous dopant distribution, as shown in b). The mean dopant incorporation efficacy is  $3.6 \cdot 10^4$   $(atoms/cm^3)/(ion/cm^2)$ .

the rotation of the profile shown in 4.1a. Irradiation with a single, relatively low ion energy produces a homogeneous doping profile.

As lower energy ions have lower ranges, there are fewer paths that cause the ion to leave the nanowire, particularly in the forward direction. Therefore, the first advantage of decreasing the ion energy is that the doping efficacy is larger for lower ion energies, so a lower irradiation fluence is required to achieve doping at a desired concentration. Furthermore, lower ion energy impacts also produce less damage in the irradiated matrix. Together with an optimal irradiation temperature, the rotated irradiation was utilized to improve the magnetic properties of  $Mn^+$  irradiated  $GaAs$  nanowires in references [BMB<sup>11</sup>, PKB<sup>12</sup>, Bor12, KPJ<sup>13</sup>, PKJ<sup>14</sup>].

## 4.2 nano-XRF on single nanowires

The increase in doping concentration with the irradiated ion fluence was investigated on  $ZnO$  nanowire samples grown in Jena. The samples such as the one shown in figure 3.1a show an upstanding, dense forest of nanowires on the growth substrate. The nanowires were rotated during the irradiation with  $0.24, 0.48, 0.95$  and  $1.9 \cdot 10^{17} ions/cm^2$   $Mn^+$  ions at  $175\text{ keV}$ ; corresponding to  $Mn/Zn$  ratios of  $0.02, 0.04, 0.08$  and  $0.16$ , as extrapolated from the mean

#### 4.2 nano-XRF on single nanowires

doping efficacy obtained from the *iradina* simulation. After the irradiation, they were transferred onto the *C*-foil of a *Cu*-TEM grid by imprinting after the

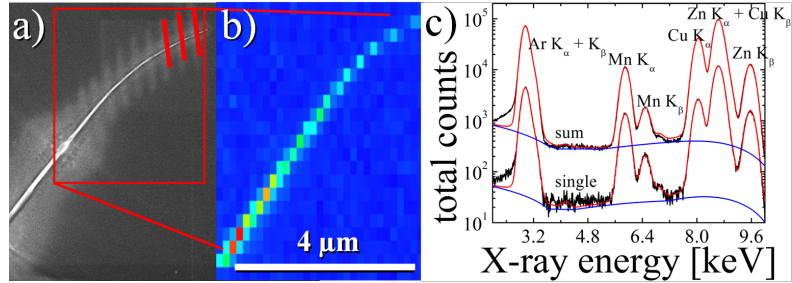


Figure 4.2: a) SEM image of a  $175\text{ keV}$   $Mn^+$  irradiated  $ZnO$  nanowire on the carbon-foil of a  $Cu$  TEM grid after XRF investigation. The red lines indicate where the focused X-ray beam was scanned with a long integration time. b) Intensity map of the X-ray signal from the nanowire shown in a). The black lines in c) show exemplary measured XRF-spectra of a single scanned line and for the sum of all the lines for the nanowire shown in a) and b). The fitted background and XRF-spectra are shown by blue and red lines.

Figure 4.2a shows a SEM image of one of the  $Mn^+$  irradiated  $ZnO$  nanowires after investigation by nano-XRF at the ESRF. At one point the nanowire shows some damage where the exposure to the XRF-beam was prolonged during the navigation on the sample. Also the track of the intense, focused X-ray beam can be seen on the carbon foil by some redeposition of material. All in all, the damage to the nanowire is, however, not large enough to have an effect on the quantification, especially considering that this particular nanowire was selected because it showed the most pronounced effects. In figure 4.2b a map of the detected X-ray intensity clearly shows the nanowire. The XRF spectrum collected for one of the scans indicated in the SEM image 4.2a is shown in 4.2c. The number of counts for a single scan is comfortably sufficient to quantify the  $Mn$  and  $Zn$  content. The average concentration for a nanowire was determined by fitting the sum XRF-spectrum of all scans across the nanowire.

In figure 4.3a the  $Mn/Zn$  ratio is plotted over the position along the nanowires' length for the four nominal concentrations. Clearly there is a significant gradient in the  $Mn$  concentration along the nanowire length. The maximum

#### 4 High Doping Concentrations in Nanowires

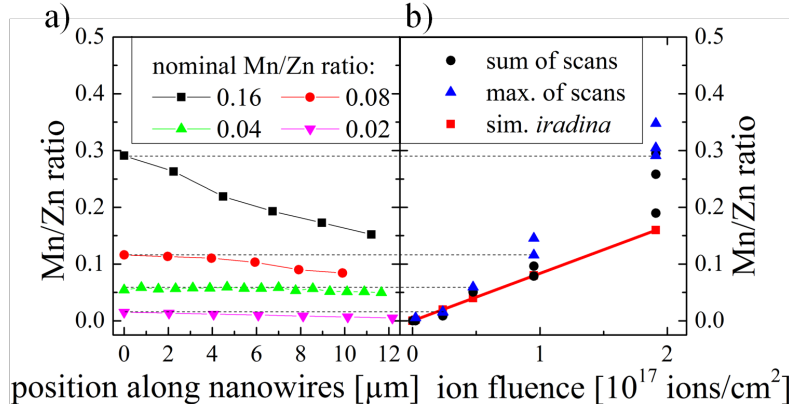


Figure 4.3: a)  $Mn/Zn$  ratio quantified with PyMCA for representative wires along the length of the nanowires for varying nominal concentrations. The tip of the nanowires is found at  $0\mu m$ . In b) the black circles show the average ratio obtained for various nanowires by fitting to the sum of all scans. The blue upturned triangles show the maximum ratio found along the length of the nanowires. The corresponding data points in the plot of the concentration versus the length of the nanowire in a) are connected with a dashed line. The red data points and line in b) indicate the linear extrapolation to the nominal  $Mn/Zn$  ratio from *iradina* simulations.

$Mn/Zn$  ratio was always found at the tip of the nanowires, the tip being identifiable in the SEM images by the slight tapering of the nanowires. The  $Mn/Zn$  ratio for both the sum of all scans, as well as the scan at the tip showing the maximum  $Mn/Zn$  ratio, is plotted in 4.3b alongside the nominal ratio extrapolated from *iradina* simulations.

Two pieces of information can be gained from these results. First, the nanowires on the sample clearly shadowed each other from the ion beam, leading to the pronounced  $Mn$  concentration gradient along the wires' length. The shadowing is least at the tips of the nanowires, therefore these points correspond closest to the simulated situation. The second point is that the increase in  $Mn$  concentration with the ion fluence is much stronger than the linear extrapolation from static simulations. Using the doping efficacy gained from the earlier simulations to calculate the required fluence for a desired doping concentration assumes, that the concentration increases linearly with the irradiated fluence. However, this is only true in the absence of sputtering. Sputtering erodes the target nanowire at the same time as ions are incorporated. It thus leads

#### 4.2 nano-XRF on single nanowires

to a non-linear increase in the concentration of dopants with the irradiated fluence. To separate the effect of shadowing amongst the nanowires from the sputtering of each individual nanowire, the irradiation and quantification has to be repeated with nanowires with a sparser lateral distribution, as shown in figure 3.1b. These were kindly provided by Dr. Helena Franke from the University Leipzig.

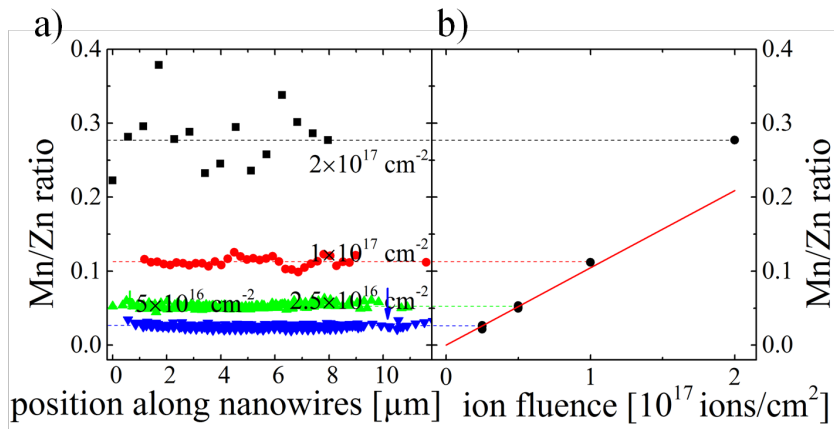


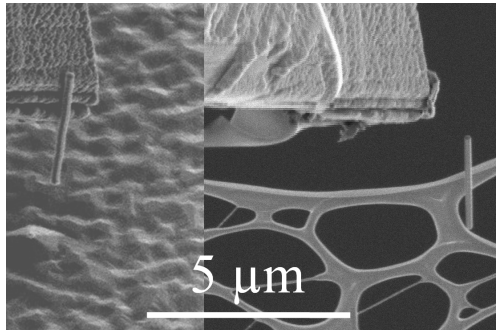
Figure 4.4: a)  $Mn/Zn$  ratio along the wire length for sparse nanowire samples irradiated with the indicated ion fluence of  $175 \text{ keV } Mn^+$ . There is no concentration profile along the wire length. In b) the average ratio obtained by fitting to the sum of all scans for the respective ion fluence is shown. The red line in b) shows the linear extrapolation from *iradina* simulations.

The same nano-XRF quantification procedure was followed to investigate the  $Mn/Zn$  ratio after the irradiation of these sparser nanowire samples with  $0.25, 0.5, 1$  and  $2 \cdot 10^{17} \text{ ions/cm}^2$  of  $175 \text{ keV } Mn^+$ . The results are shown in figure 4.4. The  $Mn/Zn$  ratios plotted against the nanowire length in 4.4a no longer show any gradient. The  $Mn/Zn$  ratio for the nanowires irradiated with higher fluences shows a significant spread due to the fact that the thinned nanowires have a much smaller volume and thus give a lower XRF signal. Added to this, the thinner wires could only be attached to the lacy carbon loosely, so that they drifted much more during the XRF scans making it impossible to increase the integration time significantly to compensate for the lower signal.

As shown in figure 4.5, these wires were individually transferred to the lacy carbon TEM grid so that nanowires, which were investigated by SEM before and after irradiation, could be selected. For example, the diameter of

#### 4 High Doping Concentrations in Nanowires

Figure 4.5: SEM images showing a ZnO nanowire broken off the growth substrate (left) with a micro-manipulator and transferred onto the lacy carbon-foil on a commercial TEM grid (right). Using this technique, individual nanowires investigated by SEM before and after the irradiation could be selected for subsequent nano-XRF quantification.



the nanowire irradiated with the highest fluence was reduced from  $202\text{ nm}$  to  $93\text{ nm}$  by sputtering. The nanowires irradiated with lower fluences showed lower reductions in their diameters, as expected. From these diameter reductions the sputter yield can be calculated, yielding sputter yields in the range of  $5 - 20\text{ atoms/ion}$ . As seen in the dedicated study on sputtering these values have a very large spread.

The average  $Mn/Zn$  ratio is plotted in 4.4b against the irradiated fluence for all irradiated fluences. It is accurate to within  $\pm 0.01$ , as it is based on the sum of the spectra of all the individual scans. This sum-spectrum includes a sufficiently large number of counts in all instances. The initial increase in the  $Mn/Zn$  ratio with the irradiated ion fluence closely follows the linear extrapolation from the doping efficacy for fluences up to  $0.5 \cdot 10^{17}\text{ ions/cm}^2$ . This is an important result, as it confirms that the MC BCA simulation can accurately predict the incorporation of dopants quantitatively. Therefore the doping efficacy is a useful number to determine the required ion fluence for a desired doping concentration for low fluences, where sputtering is not yet significant. However, as with the denser nanowire sample, for high fluences the increase in the  $Mn$  concentration is much larger than the simple linear extrapolation from the *iradina* simulation. The fact that there is no longer a gradient in the concentration along the nanowire length for the sparser samples confirms that the previously observed, strong gradient in the incorporation was caused by the shadowing of the nanowires amongst themselves.

### 4.3 Pseudo-dynamic simulation

The direct simulation of the effect of sputtering on the incorporation of dopants into nanowires requires a dynamic simulation program which also considers the three dimensional geometry of the target. As such software is not currently openly available, a step-by-step investigation using results from static simulations will be undertaken to discuss the observed interaction between dopant incorporation and sputtering.

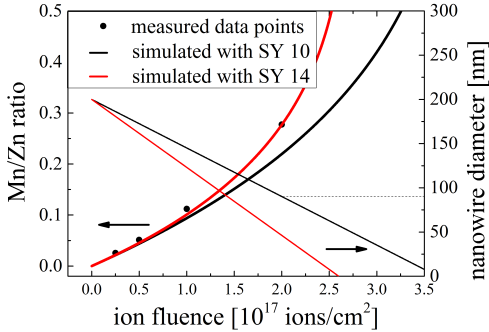


Figure 4.6: Plot of the  $Mn/Zn$  ratio (left axis) versus the irradiated ion fluence of  $175\text{ keV}Mn^+$  for the measured nanowires and two simulations using different sputter yields. The nanowire diameter (right axis) is also plotted against the fluence for both simulations. The dashed line at  $90\text{ nm}$  marks the final radius of the data point corresponding to the highest irradiated fluence.

The most straightforward approach is to consider the total sputter yield and the doping efficacy to be constant. With these assumptions and a reiterative calculation of incremental fluence steps, a pseudo-dynamic simulation can be numerically constructed. The  $Mn$  concentration increases with each irradiated incremental fluence step by the value determined by the doping efficacy. Then the number of  $Zn$ ,  $O$  and  $Mn$  atoms is reduced by sputtering in such a way, that the total sputter yield is divided between  $Zn+O$  and  $Mn$  according to the current  $Mn$  concentration. The total number of atoms is used to calculate the new nanowire radius and the next incremental fluence step can be calculated. Figure 4.6 shows the experimentally determined  $Mn/Zn$  ratios next to such a simulation. The doping efficacy was set to the same value used for the linear extrapolation so far:  $3.6 \cdot 10^4 (\text{atoms}/\text{cm}^3)/(\text{ion}/\text{cm}^2)$ . The total sputter yield was set to  $10 \text{ atoms/ion}$  for the simulation yielding the values depicted in black. This sputter yield value corresponds to the sputter yield determined from the reduction in the radius of the nanowire irradiated with  $2 \cdot 10^{17} \text{ ions/cm}^2$  and therefore, unsurprisingly, this simulation produces the the correct diameter of  $\approx 90\text{ nm}$  at this ion fluence. However, the calculated

#### 4 High Doping Concentrations in Nanowires

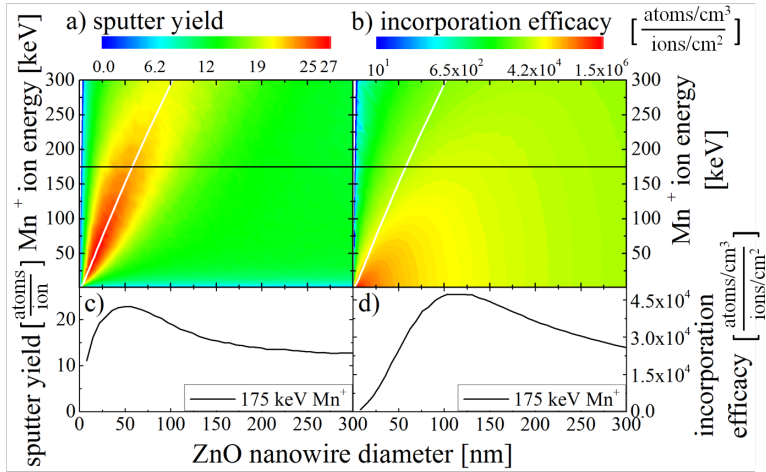


Figure 4.7: a) Sputter yield for the irradiation with  $Mn^+$  of ZnO nanowires with varying diameters and ion energies. From the same simulations the dopant incorporation efficacy was determined and plotted in b). The white line in both plots indicates the ion range at the respective energy and  $45^\circ$ , calculated with SRIM for  $Mn^+$  in  $ZnO$ . The horizontal black line indicates the ion energy used in the experiments and simulations in this chapter. For this energy the diameter-dependent sputter yield and doping efficacy are plotted in c) and d) respectively.

$Mn/Zn$  ratio is too low. Conversely, a simulation with a larger sputter yield of 14 atoms/ion, indicated in red, correctly reproduces the  $Mn/Zn$  ratio, but erodes the nanowire too quickly. Nevertheless, the overall agreement between the experiment and the simulation seems promising and confirms that the super linear increase in the doping concentration observed in the experiment can be explained by the sputtering of the nanowire.

To increase the accuracy of the pseudo-dynamic simulation, results from a set of static simulations for varying diameters can be used. The sputter yield is dependent on the nanowire radius and the ion energy as shown in figures 4.7a and 4.7c. This relation is discussed in detail in the previous chapter ???. Likewise, the incorporation efficacy plotted in 4.7b is also dependent on the nanowire radius and the ion energy. For a fixed diameter and increasing ion energy the efficacy is monotonically decreasing, as the probability of the ion to leave the nanostructure rises together with the ion range. For a fixed ion energy, as shown in figure 4.7d, the probability of an ion to stay in the nanostructure increases with increasing nanowire diameter, so that for small

### 4.3 Pseudo-dynamic simulation

diameters the efficacy also increases with increasing diameter. For large diameters this effect is overcompensated by a stronger dilution of the dopants in the volume of the nanowire which increases as the square of the diameter. This leads to a maximum in the incorporation efficacy at diameters around twice the ion range. Note that the color scale in 4.7b is logarithmic, while the graph 4.7d has a linear scale.

The numerical, pseudo-dynamic simulation can easily be adapted to use the diameter-dependent values for the sputter yield and the dopant incorporation efficacy of figures 4.7c and 4.7d. As with the previous pseudo-dynamic simulation, which only considered constant sputtering and dopant incorporation efficacy, it is only possible to reproduce the correct diameter *or* the  $Mn/Zn$  ratio. For the results shown in figure 4.8 the diameter-dependent sputter yield used for the simulation had to be halved. A simulation with the full sputter yield shown in figures 4.7c already eroded the 200 nm nanowire completely after the irradiation with an ion fluence of  $\approx 1.5 \cdot 10^{17} \text{ ions/cm}^2$ . This is not a cause for concern, however, because the quantitative values for the sputter yield obtained by *iradina* simulations are not expected to be reliable and the effective sputter yield will be reduced in a material which can (re)-oxidize. Both these points were already discussed in chapter ??.

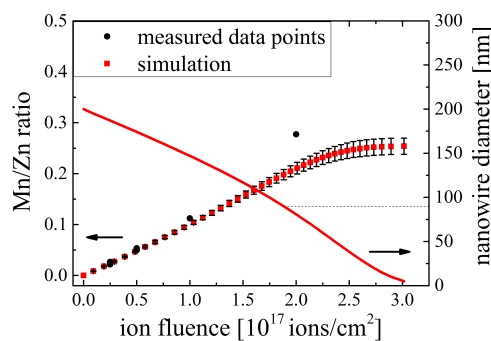


Figure 4.8: Results from a pseudo-dynamic simulation considering diameter-dependent sputtering and doping efficacy. The  $Mn/Zn$  ratio is plotted to the left axis versus the ion fluence of  $175 \text{ keV} Mn^+$  as red squares for the simulation and black circles for the experiment. The error bars range from the  $Mn/Zn$  ratio for  $170 \text{ keV}$  to  $180 \text{ keV} Mn^+$ . The red line indicates the simulated nanowire diameter.

The resulting  $Mn/Zn$  ratios from such a simulation are plotted in figure 4.8 as red squares. The stronger than linear increase in the  $Mn/Zn$  ratio with the irradiated ion fluence is offset by the doping efficacy decreasing markedly with increasing ion fluence from  $\approx 1.5 \cdot 10^{17} \text{ ions/cm}^2$ . Here the nanowire as

#### 4 High Doping Concentrations in Nanowires

a remaining diameter of around  $120\text{ nm}$ . At this diameter, the  $175\text{ keV Mn}^+$  ions start to reach the back of the now thinned nanowire, the sputtering increases and the doping efficacy decreases, as shown in figures 4.7c and 4.7d. In the evolution of the diameter with the irradiated ion fluence, plotted in figure 4.8 as a red line, the increased sputter yield is noticeable as a slight increase in the slope of the curve at  $2 \cdot 10^{17}\text{ ions/cm}^2$ .

Largely due to the reduced *Mn* incorporation in thinned nanowires, the simulation fails to reproduce the measured *Mn/Zn* ratio for ion fluences of  $1 \cdot 10^{17}\text{ ions/cm}^2$  and above, underestimating the *Mn* concentration significantly. This is due to the assumption that the probability of sputtering a *Mn* or a *Zn/O* atom is determined by the average *Mn* concentration in the nanowire. This would only be true if the doping profile were truly homogeneous. In reality there is a *Mn* poor surface region in the doping profile shown in figure 4.1b. In addition, as the nanowire is thinned during the irradiation, the homogeneity of the doping profile will also suffer. A peak emerges in the middle of the nanowire as the radius becomes equal to the ion range and smaller. In summary this means that more *Zn* and *O* atoms are sputtered from the nanowire than predicted by the *Mn* concentration weighted sputter yield and that the core is enriched in *Mn* slightly faster than the averaged doping incorporation efficacy would suggest. When the outer *Mn* poor layers of the nanowire are sputtered away the *Mn/Zn* ratio averaged over the whole cross-section increases, even without the additional incorporation of *Mn*. At this point it no longer makes sense to try to predict doping concentrations with static simulations which cannot take into account the change in the target composition and geometry. Dynamic simulations are required.

### 4.4 Summarizing Discussion

The incorporation of dopants into nanowires was studied by investigating *Mn* irradiated *ZnO* nanowires with nano-XRF. The first, perhaps slightly obvious result is that the doping concentration can be significantly influenced by shadowing of the nanowires amongst themselves. This sets some limits on the suitability of samples for homogeneous irradiation. The dense and disordered samples investigated in previous work on ion irradiated nanowires [GSM<sup>+08</sup>, RBGN10, KCG<sup>+11</sup>, Geb12, GRK<sup>+13</sup>, KGG<sup>+13</sup>, GLdR<sup>+14</sup>, CMCSR<sup>+14</sup>] for

#### 4.4 Summarizing Discussion

example, are very likely to show a large spread in the locally realized doping concentration. Related to this fact is the insight that control of the irradiation geometry can greatly reduce both the energy and ion fluence required to obtain a homogeneous doping concentration. The possibility of irradiation from different angles was realized in the presented case by rotation of the target. Both a reduced energy and a reduced ion fluence reduce the total damage produced in the target and can elevate the annealing requirements and thus improve the properties of doped nanowires [BMB<sup>+</sup>11, PKB<sup>+</sup>12, Bor12, KPJ<sup>+</sup>13, PKJ<sup>+</sup>14]. In any case, it was already shown that irradiated nanowires can bend in either direction relative to the ion beam, depending on the ion energy [BSL<sup>+</sup>11]. The rotated irradiation is a practicable alternative to complex modulations of the ion energy which could also prevent unwanted bending of nanowires during the irradiation with high fluences.

The quantification of the dopants in irradiated nanowires showed that the static MC BCA code *iradina* is accurate in the prediction the doping concentration for low ion fluences. This was expected from the discussion in chapter 2.2 on the underlying scientific background for the direct simulation of ion trajectories which translates well into nanostructures and thus naturally gives an accurate prediction of the final distribution of the ions in the target. However, a reasonable upper limit to the applicability of static simulations seems to be given in these experiments by a fluence of  $0.5 \cdot 10^{17} \text{ ions/cm}^2$ . This corresponds to the reduction of the nanowires diameter by about 10%, or a reduction of the nanowire volume by roughly 20%. Note, that this result can be generalized to other target materials, ion species and ion energies only if the ion range is comparable or larger than the nanowire diameter. For low ion energy irradiation, where the ion range is also low, the sputtering will effect the doped volume of the nanowire much sooner! The same holds true for other nanostructured geometries. A dynamic simulation is required once the sputtered layers amount to a sizable portion of either the implanted ion range or of the characteristic nanostructure length, which ever is smaller.

For flat target geometries, dynamic simulation tools have been available for some time [ME84, MEB88] and comparisons between simulations and experiments in studies on high fluence irradiation in thin layers and bulk targets have already observed the influence of sputtering on the doping concentration [MIS<sup>+</sup>91, SO93]. Unlike in nanowires, the material lost to sputtering is in-

## *4 High Doping Concentrations in Nanowires*

significant to the total bulk volume. As with irradiations of nanostructures with low ion energies, the sputtered depth has to be compared with ion range. When both become comparable, the interplay between sputtering and incorporation depth of dopants can lead to strong dynamics, including an oscillation of the dopant concentration along the depth of the target [Eck00].

Unfortunately, there is no straightforward way to extend the usefulness of static simulations to higher ion fluences. Although the attempted pseudo-dynamic simulations were partly able to reproduce the incorporated doping concentration or the nanowire radius, this was only possible in retrospect and by altering the simulation parameters. A predictive algorithm that is not dynamic was not found. The problem caused by the inhomogeneous incorporation of the dopant and the disproportionately large sputtering of the nanowire material can only be solved by dynamic codes which consider both the nanostructure geometry as well as the local concentration of each element in the target geometry. Such simulation tools are under development, if not openly available yet [Mö14].

Even in dynamic simulations, a remaining problem is posed by the sputter yield which is not easy to simulate correctly. The case for single element materials was discussed in chapter ?? on sputtering, but in compound or highly doped materials, the problem is significantly complicated by the possibility of preferential sputtering of specific elements. In flat geometries, both the preferential sputtering of the incorporated dopant, as well as compositional changes in compounds and alloys can drastically change the final composition of the irradiated layer [?, ME84, And86, MEB88, SO93, ZS95]. Due to preferential sputtering, an irradiated nanowire of a compound material may already be deficient in one of its components before a high dopant concentration is reached. At least in bulk samples the evolution of the concentration profiles for high fluence irradiations have a steady state solution. Because of mass conservation, the composition of the sputtered material is ultimately equal to the bulk material composition which lies underneath an unstoichiometric layer effected by the irradiation [And86]. Nanowires and other nanostructures, on the other hand, are destroyed by sputtering and steady state conditions cannot arise for high fluences. The evolution of their composition for high fluence irradiation is therefore much less predictable.

## 5 Conclusions and Outlook

The first conclusion, although it is actually almost a premise to this dissertation, is that sputtering is indeed an important effect that needs considering in high-fluence irradiation. As was shown in this dissertation for the example of *Si*-nanowires, this is especially the case for nanostructures, where sputter yields can be greatly enhanced. Qualitatively, a good estimation, or intuition, of how any given nanostructure will be sputtered can be obtained using the Sigmund model for sputtering. The relative size of overlap of the nuclear energy loss of the ion and the surface of the target, even if it is nanostructured, is a reasonable estimation for the relative sputter yield. Thus a feeling for which part of a complicated nanostructure will be most affected by sputtering during the irradiation with ions of a certain species and energy can be gained. For a specific nanoscaled geometry the MC BCA simulation program *iradina* [BR11] can be used to make a more detailed analysis. The diameter dependence of the simulated sputter yield is confirmed by the experiments performed in this thesis.

The quantitative values of sputtering are, in general, not accessible through the naive use of MC BCA simulations. However, very good agreement can be found for certain material and ion combinations [Bie87, HZM14], so the situation is not at all hopeless. The main difficulty is to find correct low energy interaction potential for the given situation. As the secondary ion mass spectrometry (SIMS) technique is highly reliant on sputter yields and MD simulations also require the correct interaction potential at low particle energies, there is some interest in solving this problem. *Finnland antwortet* As sputtering is dominated by low energy collisions, it is very sensitive to the interaction potential precisely at the energy range where it is not easily accessible to other experiments. Experiments on sputtering of defined nanostructures, such as the ones performed on nanowires within this thesis, may be a useful approach to test theoretical predictions based

## 5 Conclusions and Outlook

on different interaction potentials. Such experiments should be combined and compared with angle dependent measurements of the sputtering [HZM14] and the angle resolved emission of the sputtered atoms [?, ?].

The main goal of ion irradiation is typically not sputtering, but the incorporation of dopants in the target. For nanostructured targets, care has to be taken to avoid an inhomogeneous irradiation and doping profile due to shadowing of the ion beam. This was illustrated with the nano-XRF investigation of *Mn*-doped *ZnO* nanowires. The first new result from this investigation is that the BC MCA simulation is adequate for the prediction of the doping concentration for low ion fluences in nanowires. The limit of this applicability is given by the point where around 20% of the material affected by the ion beam is sputtered, which in nanostructures is typically 20% of the whole nanostructures' volume. Similar approximations can be made in bulk [ME84, And86, MEB88, SO93, ZS95], even if the given references don't explicitly state a limit at the fluence, where the depth of material sputtered is equal to 20% of the ion range. For irradiations with higher fluences dynamic simulations are needed to predict the correct dopant concentration and profile. For nanostructures this ion fluence can be much lower than in bulk as there is less material to be sputtered and sputtering is enhanced. Software, which can dynamically change the structure and composition of the ion irradiated, nanostructured target, has been revealed recently in reference [Mö14]. A comparison of the experimental results presented in this thesis with the results from such a simulation is a logical next step.

Down these lines, the application of the nano-XRF quantification technique to ion irradiated nanostructures can produce further interesting results. As it is highly sensitive to elemental concentrations, it can widen the scope of the proposed studies into sputtering by investigating compositional changes ion irradiated nanostructures of compound materials. In compound materials preferential sputtering of one of the materials' components may become relevant even before a high dopant concentration has been reached. The interplay of nano-structuring, compositional changes and preferential sputtering could thus be investigated for a vast array of materials, by no means limited to semiconductors. Comparison to simulation results would further the understanding of the parameters influencing the preferential sputtering, which has practical meaning in SIMS, but also in the development of materials for fusion

reactor components [?, ?, ?]. Using nanowires for such an experiment has the advantage that samples with multiple diameters can be fabricated in parallel and thus a larger parameter space becomes accessible.

*sputter yield units check: Master Thesis  
Noack, Ogrisek, Conference proceeding D.  
Sage, Rutherford, Nordlund*

# Bibliography

- [ABU15] Christian Anders, Eduardo M. Bringa, and Herbert M. Urbassek. Sputtering of a metal nanofoam by Au ions. *Nuclear Instruments and Methods in Physics Research Section B: Beam Interactions with Materials and Atoms*, 342:234–239, January 2015. 00000.
- [And86] Hans Henrik Andersen. Computer simulations of atomic collisions in solids with special emphasis on sputtering. *Nuclear Instruments and Methods in Physics Research Section B: Beam Interactions with Materials and Atoms*, 18(1-6):321–343, January 1986.
- [ANNK02] Karsten Albe, Kai Nordlund, Janne Nord, and Antti Kuronen. Modeling of compound semiconductors: Analytical bond-order potential for Ga, As, and GaAs. *Physical Review B*, 66(3):035205, July 2002.
- [ASS69] Hh Andersen, H. Simonsen, and H. Sorensen. An Experimental Investigation of Charge-Dependent Deviations from Bethe Stopping Power Formula. *Nuclear Physics A*, A125(1):171–&, 1969. WOS:A1969C725100012.
- [AW59] B. J. Alder and T. E. Wainwright. Studies in Molecular Dynamics. I. General Method. *The Journal of Chemical Physics*, 31(2):459–466, August 1959. 01183.
- [BD14] Richard E. Baumer and Michael J. Demkowicz. Prediction of Spontaneous Plastic Deformation of Irradiated Metallic Glasses due to Thermal Spike-Induced Plasticity. *Materials Research Letters*, 2(4):221–226, October 2014.

## Bibliography

- [Bet30] H. Bethe. Zur Theorie des Durchgangs schneller Korpuskularstrahlen durch Materie. *Annalen der Physik*, 397(3):325–400, January 1930.
- [BFS<sup>+</sup>12] Stuart A. Boden, Thomas M.W. Franklin, Larry Scipioni, Darren M. Bagnall, and Harvey N. Rutt. Ionoluminescence in the Helium Ion Microscope. *Microscopy and Microanalysis*, 18(06):1253–1262, December 2012.
- [BH88] R. Mark Bradley and James M. E. Harper. Theory of ripple topography induced by ion bombardment. *Journal of Vacuum Science & Technology A*, 6(4):2390–2395, July 1988.
- [Bie87] J. P. Biersack. Computer simulations of sputtering. *Nuclear Instruments and Methods in Physics Research Section B: Beam Interactions with Materials and Atoms*, 27(1):21–36, June 1987.
- [Blo33] F. Bloch. Zur Bremsung rasch bewegter Teilchen beim Durchgang durch Materie. *Annalen der Physik*, 408(3):285–320, January 1933.
- [BMB<sup>+</sup>11] Christian Borschel, Maria E. Messing, Magnus T. Borgstrom, Waldomiro Paschoal, Jesper Wallentin, Sandeep Kumar, Kilian Mergenthaler, Knut Deppert, Carlo M. Canali, Hakan Pettersson, Lars Samuelson, and Carsten Ronning. A New Route toward Semiconductor Nanospintronics: Highly Mn-Doped GaAs Nanowires Realized by Ion-Implantation under Dynamic Annealing Conditions. *Nano Letters*, 11(9):3935–3940, September 2011. WOS:000294790200073.
- [BMS<sup>+</sup>06] C. Borchers, S. Müller, D. Stichtenoth, D. Schwen, and C. Ronning. Catalyst Nanostructure Interaction in the Growth of 1d ZnO Nanostructures. *The Journal of Physical Chemistry B*, 110(4):1656–1660, February 2006.
- [BMS<sup>+</sup>08] Ivan Bizyukov, Andreas Mutzke, Ralf Schneider, Alexander M. Gigler, and Karl Krieger. Morphology and changes of elemental surface composition of tungsten bombarded with carbon ions.

## Bibliography

*Nuclear Instruments and Methods in Physics Research Section B: Beam Interactions with Materials and Atoms*, 266(9):1979–1986, May 2008. 00007.

- [Bor12] Christian Borschel. *Ion-Solid Interaction in Semiconductor Nanowires*. PhD thesis, University Jena, Jena, 2012.
- [BR11] C. Borschel and C. Ronning. Ion beam irradiation of nano-structures – A 3d Monte Carlo simulation code. *Nuclear Instruments and Methods in Physics Research Section B: Beam Interactions with Materials and Atoms*, 269(19):2133–2138, October 2011.
- [BSL<sup>+</sup>11] Christian Borschel, Susann Spindler, Damiana Lerose, Arne Bochmann, Silke H. Christiansen, Sandor Nietzsche, Michael Oertel, and Carsten Ronning. Permanent bending and alignment of ZnO nanowires. *Nanotechnology*, 22(18):185307, May 2011. WOS:000288653300010.
- [CMCSR<sup>+</sup>14] M. H. Chu, G. Martínez-Criado, J. Segura-Ruiz, S. Geburt, and C. Ronning. Nano-X-ray diffraction study of single Co-implanted ZnO nanowires: Nano-X-ray diffraction study of single NWs. *physica status solidi (a)*, 211(11):2523–2526, November 2014.
- [CW65] J. W. Corbett and G. D. Watkins. Production of Divacancies and Vacancies by Electron Irradiation of Silicon. *Physical Review*, 138(2A):A555–A560, April 1965.
- [CZC<sup>+</sup>10] B. Q. Cao, J. Zuniga-Perez, C. Czekalla, H. Hilmer, J. Lenzner, N. Boukos, A. Travlos, M. Lorenz, and M. Grundmann. Tuning the lateral density of ZnO nanowire arrays and its application as physical templates for radial nanowire heterostructures. *Journal of Materials Chemistry*, 20(19):3848–3854, May 2010.
- [Ded95] Gv Dedkov. The Interatomic Interaction Potentials in Radiation Physics. *Physica Status Solidi a-Applications and Materials Science*, 149(2):453–513, June 1995. WOS:A1995RH61400001.

## Bibliography

- [Dha07] S. Dhara. Formation, dynamics, and characterization of nanostructures by ion beam irradiation. *Critical Reviews in Solid State and Materials Sciences*, 32(1-2):1–50, 2007. WOS:000247237500001.
- [DL00] X. Duan and C. M. Lieber. General Synthesis of Compound Semiconductor Nanowires. *Advanced Materials*, 12(4):298–302, February 2000.
- [Eck91] Wolfgang Eckstein. *Computer Simulation of Ion-Solid Interactions*. Springer Berlin Heidelberg, Berlin, Heidelberg, 1991.
- [Eck00] W Eckstein. Oscillations of sputtering yield. *Nuclear Instruments and Methods in Physics Research Section B: Beam Interactions with Materials and Atoms*, 171(4):435–442, December 2000.
- [EHHF92] W. Eckstein, S. Hackel, D. Heinemann, and B. Fricke. Influence of the Interaction Potential on Simulated Sputtering and Reflection Data. *Zeitschrift Fur Physik D-Atoms Molecules and Clusters*, 24(2):171–176, September 1992. WOS:A1992JQ04000013.
- [FH13] Brent Fultz and James Howe. *Transmission Electron Microscopy and Diffractometry of Materials*. Graduate Texts in Physics. Springer Berlin Heidelberg, Berlin, Heidelberg, 2013.
- [Fur88] J. K. Furdyna. Diluted magnetic semiconductors. *Journal of Applied Physics*, 64(4):R29–R64, August 1988.
- [Geb12] Sebastian Geburt. *Lasing and ion beam doping of semiconductor nanowires*. PhD thesis, University Jena, Jena, 2012.
- [GHB<sup>+</sup>13] G. Greaves, J. A. Hinks, P. Busby, N. J. Mellors, A. Ilinov, A. Kuronen, K. Nordlund, and S. E. Donnelly. Enhanced Sputtering Yields from Single-Ion Impacts on Gold Nanorods. *Physical Review Letters*, 111(6):065504, August 2013. 00004.
- [GLdR<sup>+</sup>14] Sebastian Geburt, Michael Lorke, Andreia L. da Rosa, Thomas Frauenheim, Robert Röder, Tobias Voss, Uwe Kaiser, Wolfram

## Bibliography

- Heimbrodt, and Carsten Ronning. Intense Intrashell Luminescence of Eu-Doped Single ZnO Nanowires at Room Temperature by Implantation Created Eu–O<sub>i</sub> Complexes. *Nano Letters*, 14(8):4523–4528, August 2014.
- [GRK<sup>+</sup>13] Sebastian Geburt, Robert Röder, Uwe Kaiser, Limei Chen, Manh-Hung Chu, Jaime Segura-Ruiz, Gema Martínez-Criado, Wolfram Heimbrodt, and Carsten Ronning. Intense intra-3d luminescence and waveguide properties of single Co-doped ZnO nanowires: Intense intra-3d luminescence and waveguide properties of single Co-doped ZnO nanowires. *physica status solidi (RRL) - Rapid Research Letters*, 7(10):886–889, October 2013.
- [GS28] R. Glocke and H. Schreiber. Quantitative Röntgenspektralanalyse mit Kalterregung des Spektrums. *Annalen der Physik*, 390(8):1089–1102, January 1928.
- [GSM<sup>+</sup>08] S. Geburt, D. Stichtenoth, S. Müller, W. Dewald, C. Ronning, J. Wang, Y. Jiao, Y. Y. Rao, S. K. Hark, and Quan Li. Rare Earth Doped Zinc Oxide Nanowires. *Journal of Nanoscience and Nanotechnology*, 8(1):244–251, January 2008.
- [Hau84] M. Hautala. Nuclear stopping in polycrystalline materials: Range distributions and Doppler-shift attenuation analysis. *Physical Review B*, 30(9):5010–5018, November 1984. 00059.
- [HFH<sup>+</sup>90] S. Hackel, B. Fricke, D. Heinemann, D Kolb, and L Yang. Inter-Nuclear Potential of the System Si-Si calculated with the Finite-Element-Method. *GSI Annual Report*, page 165, 1990.
- [HIK97] C. Haginoya, M. Ishibashi, and K. Koike. Nanostructure array fabrication with a size-controllable natural lithography. *Applied Physics Letters*, 71(20):2934–2936, November 1997. WOS:A1997YF67500022.
- [HKZ<sup>+</sup>10] Birgit J. M. Hausmann, Mughees Khan, Yinan Zhang, Tom M. Babinec, Katie Martinick, Murray McCutcheon, Phil R. Hemmer, and Marko Loncar. Fabrication of diamond nano-

## Bibliography

- wires for quantum information processing applications. *Diamond and Related Materials*, 19(5-6):621–629, June 2010. WOS:000278193600059.
- [HZM14] H. Hofssäss, K. Zhang, and A. Mutzke. Simulation of ion beam sputtering with SDTrimSP, TRIDYN and SRIM. *Applied Surface Science*, 310:134–141, August 2014.
- [JHMR15] Andreas Johannes, Henry Holland-Moritz, and Carsten Ronning. Ion beam irradiation of nanostructures: sputtering, dopant incorporation, and dynamic annealing. *Semiconductor Science and Technology*, 30(3):033001, March 2015.
- [JNP<sup>+</sup>14] A. Johannes, S. Noack, W. Paschoal, S. Kumar, D. Jacobsson, H. Pettersson, L. Samuelson, K. A. Dick, G. Martinez-Criado, M. Burghammer, and C. Ronning. Enhanced sputtering and incorporation of Mn in implanted GaAs and ZnO nanowires. *Journal of Physics D-Applied Physics*, 47(39):394003, October 2014. WOS:000341772000005.
- [JNW<sup>+</sup>15] Andreas Johannes, Stefan Noack, Werner Wesch, Markus Glaser, Alois Lugstein, and Carsten Ronning. Anomalous Plastic Deformation and Sputtering of Ion Irradiated Silicon Nanowires. *Nano Letters*, May 2015.
- [Jon24] J. E. Jones. On the Determination of Molecular Fields. II. From the Equation of State of a Gas. *Proceedings of the Royal Society of London A: Mathematical, Physical and Engineering Sciences*, 106(738):463–477, October 1924.
- [JS82] W. Jansen and M. Slaughter. Elemental Mapping of Minerals by Electron Micro-Probe. *American Mineralogist*, 67(5-6):521–533, 1982. WOS:A1982NZ59500008.
- [KCG<sup>+</sup>11] Uwe Kaiser, Limei Chen, Sebastian Geburt, Carsten Ronning, and Wolfram Heimbrodt. Defect induced changes on the excitation transfer dynamics in ZnS/Mn nanowires. *Nanoscale Research Letters*, 6(1):228, March 2011.

## Bibliography

- [Kel78] Roger Kelly. An attempt to understand preferential sputtering. *Nuclear Instruments and Methods*, 149(1–3):553–558, March 1978.
- [KGG<sup>+</sup>13] Uwe Kaiser, Sebastian Gies, Sebastian Geburt, Franziska Riedel, Carsten Ronning, and Wolfram Heimbrod. Luminescence and energy transfer processes in ensembles and single Mn or Tb doped ZnS nanowires. *Journal of Applied Physics*, 113(7):073506, February 2013.
- [Kik28] Seishi Kikuchi. Diffraction of Cathode Rays by Mica. *Proceedings of the Imperial Academy*, 4(6):271–274, 1928.
- [KOW11] T. Kenmotsu, T. Ono, and M. Wada. Effect of deuterium retention upon sputtering yield of tungsten by deuterons. *Journal of Nuclear Materials*, 415(1, Supplement):S108–S111, August 2011.
- [KPJ<sup>+</sup>13] Sandeep Kumar, Waldomiro Paschoal, Andreas Johannes, Daniel Jacobsson, Christian Borschel, Anna Pertsova, Chih-Han Wang, Maw-Kuen Wu, Carlo M. Canali, Carsten Ronning, Lars Samuelson, and Håkan Pettersson. Magnetic Polarons and Large Negative Magnetoresistance in GaAs Nanowires Implanted with Mn Ions. *Nano Letters*, 13(11):5079–5084, 2013.
- [Lin54] J. Lindhard. On the Properties of a Gas of Charged Particles. *Matematisk-Fysiske Meddelelser Kongelige Danske Videnskabernes Selskab*, 28(8):1–57, 1954. WOS:A1954XZ29300001.
- [LSH<sup>+</sup>08] A. Lugstein, M. Steinmair, Y. J. Hyun, G. Hauer, P. Pongratz, and E. Bertagnolli. Pressure-induced orientation control of the growth of epitaxial silicon nanowires. *Nano Letters*, 8(8):2310–2314, August 2008. WOS:000258440700034.
- [Mü09] Sven Müller. *Structural and optical impact of transition metal implantation into zinc oxide single crystals and nanowires*. PhD thesis, Georg-August Universität Göttingen, Göttingen, 2009.

## Bibliography

- [Mö14] Wolfhard Möller. TRI3dyn – Collisional computer simulation of the dynamic evolution of 3-dimensional nanostructures under ion irradiation. *Nuclear Instruments and Methods in Physics Research Section B: Beam Interactions with Materials and Atoms*, 322:23–33, March 2014. 00001.
- [ME84] W. Möller and W. Eckstein. Tridyn — A TRIM simulation code including dynamic composition changes. *Nuclear Instruments and Methods in Physics Research Section B: Beam Interactions with Materials and Atoms*, 2(1–3):814–818, March 1984.
- [MEB88] W. Möller, W. Eckstein, and J. P. Biersack. Tridyn-binary collision simulation of atomic collisions and dynamic composition changes in solids. *Computer Physics Communications*, 51(3):355–368, November 1988. 00441.
- [MIS<sup>+</sup>91] Y. Miyagawa, M. Ikeyama, K. Saito, G. Massouras, and S. Miyagawa. Computer simulation of dose effects on composition profiles under ion implantation. *Journal of Applied Physics*, 70(12):7289, 1991.
- [MK97] Antonio Miotello and Roger Kelly. Revisiting the thermal-spike concept in ion-surface interactions. *Nuclear Instruments and Methods in Physics Research Section B: Beam Interactions with Materials and Atoms*, 122(3):458–469, February 1997.
- [Mol47] G. Moliere. Theorie Der Streuung Schneller Geladener Teilchen .1. *Zeitschrift Fur Naturforschung Section a-a Journal of Physical Sciences*, 2(3):133–145, 1947. WOS:A1947UW40000002.
- [Nas08] Nastasi/Mayer/Hirvonen. *Ion-Solid Interactions: Fundamentals and Applications*. Cambridge University Press, Cambridge ; New York, auflage: revised. edition, January 2008.
- [ND08] Kai Nordlund and Sergei L. Dudarev. Interatomic potentials for simulating radiation damage effects in metals. *Comptes Rendus Physique*, 9(3–4):343–352, April 2008.

## Bibliography

- [NKA<sup>+</sup>04] Nick S. Norberg, Kevin R. Kittilstved, James E. Amonette, Ravi K. Kukkadapu, Dana A. Schwartz, and Daniel R. Gamelin. Synthesis of Colloidal Mn<sub>2+</sub>:ZnO Quantum Dots and High-TC Ferromagnetic Nanocrystalline Thin Films. *Journal of the American Chemical Society*, 126(30):9387–9398, August 2004.
- [Noa14] Stefan Noack. *Sputter Effects of Silicon Nanowires under Ion Bombardment*. University Jena, Master Thesis, 2014.
- [Nor95] K. Nordlund. Molecular dynamics simulation of ion ranges in the 1–100 keV energy range. *Computational Materials Science*, 3(4):448–456, March 1995. 00248.
- [Nor14] Kai Nordlund. Correction to the Kinchin-Phase damage equation to account for athermal defect recombination and ion beam mixing: arc-dpa and rpa. In *Oral Presentation*, Leuven, September 2014.
- [NRS97] K. Nordlund, N. Runeberg, and D. Sundholm. Repulsive interatomic potentials calculated using Hartree-Fock and density-functional theory methods. *Nuclear Instruments & Methods in Physics Research Section B-Beam Interactions with Materials and Atoms*, 132(1):45–54, October 1997. WOS:A1997YF32200007.
- [NSUM14] Maureen L. Nietiadi, Luis Sandoval, Herbert M. Urbassek, and Wolfhard Möller. Sputtering of Si nanospheres. *Physical Review B*, 90(4):045417, July 2014.
- [Ogr13] Matthias Ogrisek. *Kontrolliertes Wachstum von Zinkoxid und Vanadium(IV)-oxid Nanodrähten*. University Jena, Master Thesis, 2013.
- [Ots79] NOBUYUKI Otsu. A Threshold Selection Method from Gray-Level Histograms. *IEEE Transactions on Systems, Man, and Cybernetics*, 9(1):62–66, 1979.

## Bibliography

- [PKB<sup>+</sup>12] Waldomiro Paschoal, Sandeep Kumar, Christian Borschel, Phillip Wu, Carlo M. Canali, Carsten Ronning, Lars Samuelson, and Hakan Pettersson. Hopping Conduction in Mn Ion-Implanted GaAs Nanowires. *Nano Letters*, 12(9):4838–4842, September 2012. WOS:000308576000069.
- [PKJ<sup>+</sup>14] W. Paschoal, Sandeep Kumar, D. Jacobsson, A. Johannes, V. Jain, C. M. Canali, A. Pertsova, C. Ronning, K. A. Dick, L. Samuelson, and H. Pettersson. Magnetoresistance in Mn ion-implanted GaAs:Zn nanowires. *Applied Physics Letters*, 104(15):153112, April 2014. WOS:000335145200060.
- [PMB04] Lourdes Pelaz, Luis A. Marqués, and Juan Barbolla. Ion-beam-induced amorphization and recrystallization in silicon. *Journal of Applied Physics*, 96(11):5947–5976, December 2004.
- [RBGN10] C. Ronning, C. Borschel, S. Geburt, and R. Niepelt. Ion beam doping of semiconductor nanowires. *Materials Science and Engineering: R: Reports*, 70(3–6):30–43, November 2010.
- [Rot90] J. Roth. Sputtering of Limiter and Divertor Materials. *Journal of Nuclear Materials*, 176:132–141, December 1990. WOS:A1990FC48200014.
- [Rut11] E Rutherford. The scattering of alpha and beta particles by matter and the structure of the atom. *Philosophical Magazine Series 6*, 21(125):669–688, May 1911.
- [SACF<sup>+</sup>12] Johannes Schindelin, Ignacio Arganda-Carreras, Erwin Frise, Verena Kaynig, Mark Longair, Tobias Pietzsch, Stephan Preibisch, Curtis Rueden, Stephan Saalfeld, Benjamin Schmid, Jean-Yves Tinevez, Daniel James White, Volker Hartenstein, Kevin Eliceiri, Pavel Tomancak, and Albert Cardona. Fiji: an open-source platform for biological-image analysis. *Nature Methods*, 9(7):676–682, June 2012.
- [San04] B Sankur. Survey over image thresholding techniques and quantitative performance evaluation. *Journal of Electronic Imaging*, 13(1):146, January 2004.

## Bibliography

- [SBB53] Fm Smith, W. Birnbaum, and Wh Barkas. Measurements of Meson Masses and Related Quantities. *Physical Review*, 91(3):765–766, 1953. WOS:A1953UB46200058.
- [Sch08] François Schiettekatte. Fast Monte Carlo for ion beam analysis simulations. *Nuclear Instruments and Methods in Physics Research Section B: Beam Interactions with Materials and Atoms*, 266(8):1880–1885, April 2008.
- [Sig69] Peter Sigmund. Theory of Sputtering. I. Sputtering Yield of Amorphous and Polycrystalline Targets. *Physical Review*, 184(2):383–416, August 1969. 03204.
- [Sig73] Peter Sigmund. A mechanism of surface micro-roughening by ion bombardment. *Journal of Materials Science*, 8(11):1545–1553, November 1973.
- [Sig04] Peter Sigmund, editor. *Stopping of Heavy Ions*, volume 204 of *Springer Tracts in Modern Physics*. Springer Berlin Heidelberg, Berlin, Heidelberg, 2004.
- [SO93] Peter Sigmund and Antonino Oliva. Alloy sputtering at high fluence: preferential sputtering and competing effects. *Nuclear Instruments and Methods in Physics Research Section B: Beam Interactions with Materials and Atoms*, 82(2):269–282, July 1993.
- [SPC<sup>+</sup>07] V. A. Solé, E. Papillon, M. Cotte, Ph. Walter, and J. Susini. A multiplatform code for the analysis of energy-dispersive X-ray fluorescence spectra. *Spectrochimica Acta Part B: Atomic Spectroscopy*, 62(1):63–68, January 2007.
- [SPTS12] Daniel Sage, D. Prodanov, J.-Y. Tinevez, and J. Schindelin. ImageJ User & Developer Conference (IUDC’12). 2012.
- [SS14] Peter Sigmund and Andreas Schinner. Notes on the Barkas-Andersen effect. *European Physical Journal D. Atomic, Molecular, Optical and Plasma Physics*, 68, 2014.

## Bibliography

- [Sti08] Daniel Stichtenoth. *Dimensionseffekte in Halbleiternanodrähten*. PhD thesis, Georg-August Universität Göttingen, Göttingen, 2008.
- [SW85] Frank H. Stillinger and Thomas A. Weber. Computer simulation of local order in condensed phases of silicon. *Physical Review B*, 31(8):5262–5271, April 1985.
- [TDP92] M. Toulemonde, C. Dufour, and E. Paumier. Transient thermal process after a high-energy heavy-ion irradiation of amorphous metals and semiconductors. *Physical Review B*, 46(22):14362–14369, December 1992.
- [Ter88] J. Tersoff. New empirical approach for the structure and energy of covalent systems. *Physical Review B*, 37(12):6991–7000, April 1988.
- [Tho68] Mw Thompson. Energy Spectrum of Ejected Atoms During High Energy Sputtering of Gold. *Philosophical Magazine*, 18(152):377–&, 1968. WOS:A1968B525400015.
- [UBNM15] Herbert M. Urbassek, R. Mark Bradley, Maureen L. Nietiadi, and Wolfhard Möller. Sputter yield of curved surfaces. *Physical Review B*, 91(16):165418, April 2015.
- [VWMS08] C. Verdeil, T. Wirtz, H. N. Migeon, and H. Scherrer. Angular distribution of sputtered matter under Cs+ bombardment with oblique incidence. *Applied Surface Science*, 255(4):870–873, December 2008.
- [WDJ<sup>+</sup>09] Brent A. Wacaser, Kimberly A. Dick, Jonas Johansson, Magnus T. Borgström, Knut Deppert, and Lars Samuelson. Preferential Interface Nucleation: An Expansion of the VLS Growth Mechanism for Nanowires. *Advanced Materials*, 21(2):153–165, January 2009.
- [WE64] Rs Wagner and Wc Ellis. Vapor-Liquid-Solid Mechanism of Single Crystal Growth ( New Method Growth Catalysis from

## Bibliography

- Impurity Whisker Epitaxial + Large Crystals Si E ). *Applied Physics Letters*, 4(5):89–&, 1964. WOS:A19645163A00003.
- [WHB77] W. D. Wilson, L. G. Haggmark, and J. P. Biersack. Calculations of nuclear stopping, ranges, and straggling in the low-energy region. *Physical Review B*, 15(5):2458–2468, March 1977.
- [Wie88] E Wiedemann. Über Fluorescenz und Phosphorescenz, I. Abhandlung. *Annalen der Physik*, 34:446–463, 1888.
- [WKW04] W. Wesch, A. Kamarou, and E. Wendler. Effect of high electronic energy deposition in semiconductors. *Nuclear Instruments & Methods in Physics Research Section B-Beam Interactions with Materials and Atoms*, 225(1-2):111–128, August 2004. WOS:000223792600010.
- [WM08] T. Wirtz and H. N. Migeon. Storing Matter: A new quantitative and sensitive analytical technique. *Applied Surface Science*, 255(4):1498–1500, December 2008.
- [WWS12] W. Wesch, E. Wendler, and C. S. Schnohr. Damage evolution and amorphization in semiconductors under ion irradiation. *Nuclear Instruments and Methods in Physics Research Section B: Beam Interactions with Materials and Atoms*, 277:58–69, April 2012. 00009.
- [YS84] Y. Yamamura and Shigeru Shindo. An empirical formula for angular dependence of sputtering yields. *Radiation Effects*, 80(1-2):57–72, January 1984.
- [Zie12] James Ziegler. *SRIM - The Stopping and Range of Ions in Matter*. February 2012.
- [ZLB85] J. F. (James F. ) Ziegler, U. Littmark, and J. P. Biersack. *The stopping and range of ions in solids / J.F. Ziegler, J.P. Biersack, U. Littmark*. The Stopping and ranges of ions in matter ; v. 1. Pergamon, New York, 1985. Includes index. Bibliography: p. 308-315.

## Bibliography

- [ZS95] Vladimir I. Zaporozchenko and Maria G. Stepanova. Preferential sputtering in binary targets. *Progress in Surface Science*, 49(2):155–196, June 1995.